

Examenarbete

Development of a Beam Loss Monitoring System for CTF-3 TBL

Erik Branger

Examensarbetet utfört vid CERN

2013-08-21

LITH - IFM - A - EX - - 13/2836 - - SE



TEKNISKA HÖGSKOLAN
LINKÖPINGS UNIVERSITET

Linköpings universitet Institutionen för fysik, kemi och biologi
581 83 Linköping



Development of a Beam Loss Monitoring System for CTF-3 TBL

Erik Branger

Examensarbetet utfört vid CERN

2013-08-21

Handledare

Sophie Mallovs

Magnus Johansson

Examinator

Peter Münger



TEKNISKA HÖGSKOLAN
LINKÖPINGS UNIVERSITET

Development of a Beam Loss Monitoring system for CTF-3 TBL

Examensarbete i teknisk fysik utfört vid
Tekniska högskolan vid Linköpings universitet
av

Erik Branger

LITH - IFM - A - EX - - 13/2836 - - SE

Supervisors: **M.Sc Sophie Mallows**
CERN

Dr. Eva Barbara Holzer
CERN

Dr. Magnus Johansson
IFM, Linköpings universitet

Examiner: **Dr. Peter Münger**
IFM, Linköpings universitet



Avdelning, institution
Division, Department

Physics
Department of Physics, Chemistry and Biology
Linköping University

Datum
Date

2013-08-21

Språk
Language

- ☐ Svenska/Swedish
☒ Engelska/English

☐ _____

Rapporttyp
Report category

- ☐ Licentiatavhandling
☒ Examensarbete
☐ C-uppsats
☐ D-uppsats
☐ Övrig rapport

☐ _____

ISBN

ISRN: LITH - IFM - A - EX - - 13/2836 - - SE

Serietitel och serienummer
Title of series, numbering

ISSN

URL för elektronisk version

Titel
Title

Utveckling av ett system för att upptäcka strålförluster vid CTF-3 TBL
Development of a Beam Loss Monitoring system for CTF-3 TBL

Författare
Author

Erik Branger

Sammanfattning
Abstract

The Compact Linear Collider (CLIC) study is a feasibility study for a new linear accelerator that aims to reach a center-of-mass collision energy of 3 TeV. To keep the length of the accelerator reasonable, a high accelerating gradient of 100 MeV/m is provided by a novel acceleration scheme, where power is extracted from a high-intensity drive beam to accelerate a high-energy main beam. The Test Beam Line (TBL) at the CLIC Test Facility 3 (CTF-3) is an experimental beamline constructed to test the technology for deceleration and power extraction of the drive beam.

A Beam Loss Monitoring (BLM) system is currently under development to investigate the amount of beam loss at the TBL, with the aim of providing information about the stability of the beam under deceleration. These detectors are placed outside of the accelerator, and measure the secondary particle shower created by particles lost in the TBL. The amount of particles that can be detected by the BLM detectors was simulated using the Monte Carlo transport code FLUKA. Several different loss scenarios were simulated, in order to calculate the intensity and composition of the secondary particle shower at the detector locations. Various approximations for the sensitivity of the detectors were considered, and were combined with the simulated intensity of the shower to estimate the detector output signal per lost particle. These values were compared with data taken by the TBL BLM system, to estimate the amount of beam lost while the TBL is running.

Nyckelord
Keyword

Beam Loss Monitoring, BLM, FLUKA, CTF-3 TBL, particle detector.

Abstract

The Compact Linear Collider (CLIC) study is a feasibility study for a new linear accelerator that aims to reach a center-of-mass collision energy of 3 TeV. To keep the length of the accelerator reasonable, a high accelerating gradient of 100 MeV/m is provided by a novel acceleration scheme, where power is extracted from a high-intensity drive beam to accelerate a high-energy main beam. The Test Beam Line (TBL) at the CLIC Test Facility 3 (CTF-3) is an experimental beamline constructed to test the technology for deceleration and power extraction of the drive beam.

A Beam Loss Monitoring (BLM) system is currently under development to investigate the amount of beam loss at the TBL, with the aim of providing information about the stability of the beam under deceleration. These detectors are placed outside of the accelerator, and measure the secondary particle shower created by particles lost in the TBL. The amount of particles that can be detected by the BLM detectors was simulated using the Monte Carlo transport code FLUKA. Several different loss scenarios were simulated, in order to calculate the intensity and composition of the secondary particle shower at the detector locations. Various approximations for the sensitivity of the detectors were considered, and were combined with the simulated intensity of the shower to estimate the detector output signal per lost particle. These values were compared with data taken by the TBL BLM system, to estimate the amount of beam lost while the TBL is running.

Acknowledgements

I would especially like to thank Sophie Mallows, who has always been around to answer questions, give suggestions and guidance, and help with all parts of the work.

I would like to thank Eva Barbara Holzer, who has provided interesting discussions about the work, methods and results.

I would like to thank Manuel Zingl and Eduardo Neboto Del Busto, who have been working with similar projects, and have provided insight into the detector equipment and detection requirements.

I would like to thank everyone in the CERN BE-BI-BL section, who have provided good company and made my six months at CERN a great time.

Finally, I would like to thank Magnus Johansson and Peter Munger, who took me on as supervisor and examiner on short notice.

Notation

List of abbreviations

ACEM	Aluminium Cathode Electron Multiplier
AS	Accelerating Structure
BLM	Beam Loss Monitor
BPM	Beam Position Monitor
CLIC	Compact Linear Collider
CLEX	CLIC Experimental Hall
CTF-3	CLIC Test Facility 3
FODO	Accelerator layout with alternating focusing and defocusing magnets
MIP	Minimum Ionizing Particle
MPPC	Multi Pixel Photon Counter
PETS	Power Extraction Transfer Structure
PMT	Photomultiplier Tube
TBL	Test Beam Line
QP	Quadrupole

Contents

1	Introduction	7
2	Beam Loss Monitoring	10
2.1	Types of losses	10
2.2	Detection principles	11
2.3	Selecting an appropriate detector	12
3	The Compact Linear Collider	14
3.1	CLIC layout	16
3.1.1	Drive Beam	16
3.1.2	Main Beam	17
3.1.3	Main linac	17
3.1.4	Detectors	18
3.2	Machine protection at CLIC	18
3.3	BLM requirements at CLIC	19
3.3.1	Sensitivity and dynamic range	20
3.3.2	Temporal and spatial resolution	20
3.3.3	Life time and radiation hardness	21
3.3.4	BLMs considered for CLIC	21
3.4	CLIC Test Facility	21
3.4.1	Two Beam Test Stand	21
3.4.2	Test Beam Line	22
4	BLM equipment at CTF3	23
4.1	Installed equipment	23
4.1.1	ACEM	23
4.1.2	PEP-II	25
4.1.3	Diamond detector	25
4.1.4	Cherenkov fiber	26
4.1.5	Installation at CTF-3	28
4.2	Other proposed detectors	28
4.2.1	Ionization chambers	28
4.3	Other equipment of interest	29
4.3.1	BPM	29

4.3.2	RADMON	29
5	FLUKA model	30
5.1	TBL module	30
5.2	Quadrupole magnetic field	31
5.3	Other TBL components	31
5.4	Regions for measuring particle showers	32
5.5	Twostep method	32
5.6	Primary electron starting position	33
5.7	FLUKA physics settings	34
6	Simulated losses at quadrupoles	35
6.1	Effect of the lost electron energy on the secondary particle shower	35
6.2	Particle composition of secondary particle showers	36
6.3	Effect of the loss location on the secondary particle shower	36
6.4	Secondary particle fluence at different detector locations	38
6.5	Effects of quadrupole type	41
6.6	Effects of beam impact angle	42
6.7	Loss distribution along beamline	42
6.8	Loss scenario	45
7	Other simulated loss scenarios	47
7.1	Uniform losses along the TBL	47
7.2	Losses at BPM and PETS	47
7.3	Beam dump	48
8	Estimate of BLM signals from simulations	52
8.1	Detector settings and sensitivity	52
8.1.1	ACEM	53
8.1.2	PEP-II	53
8.1.3	Diamond	54
8.1.4	Cherenkov fiber	54
8.1.5	Estimated error	55
8.1.6	Detector sensitivity summary	56
8.2	Simulated particles at detector locations	57
8.3	Estimated BLM signal	60
9	Measurements at CTF-3	62
9.1	Conditions	62
9.2	Localized detectors	62
9.3	Cherenkov fiber	64
9.4	BPM	66
10	Conclusions	69

Chapter 1

Introduction

Developed since the middle of the previous century, the standard model explains most known phenomena in particle physics. It consists of a unified electroweak theory as well as quantum chromodynamics, thus explaining three of the fundamental forces - the electromagnetic, weak and strong force. The only force not explained by the standard model is gravity, a force that is many orders of magnitude weaker than the other forces.

The standard model has successfully explained the behaviour of the fundamental forces, and has also predicted several new particles that were later discovered. A third generation of quarks was predicted by Kobayashi and Maskawa in 1973, and these quarks, named bottom and top, were discovered in 1977 and 1995. A new boson required by the explanation of the symmetry-breaking of the electroweak force, which would explain why certain particles have mass, was proposed by Higgs in 1964, and was found in 2012 and confirmed to be a Higgs boson in 2013.

Particle accelerators are used to investigate the properties of particles, and to test the standard model. By accelerating particles to high energies and colliding them, new particles are created that can be studied. The most powerful accelerator to date, the Large Hadron Collider, accelerates protons to a center-of-mass energy of 7-8 TeV before colliding them. Since protons are not elementary particles, it is not known and cannot be controlled which constituents take part in the collisions, which limits the precision of any observations. An electron-positron collider would give better precision, since the initial states are well defined.

The Compact Linear Collider (CLIC) study is a feasibility study for a linear electron-positron collider. With a center-of-mass collision energy of up to 3 TeV, the accelerator will make precision measurements of the newly found Higgs boson, as well as continue the search for physics beyond the standard model. But for an accelerator to discover something new, it must search at higher energy ranges than previous accelerators, since collision at lower energies have already been thoroughly studied. For this reason, new accelerators are built more powerful than their predecessors. The centre-of-mass collision energy is plotted in figure 1.1 for several accelerators constructed during the past 50 years.

With the increase in beam energy, the consequences of beam losses become more severe. The LHC beam contains enough energy to melt 500 kg of copper, and if only a fraction of the beam is lost it can severely damage the accelerator. A machine protection scheme

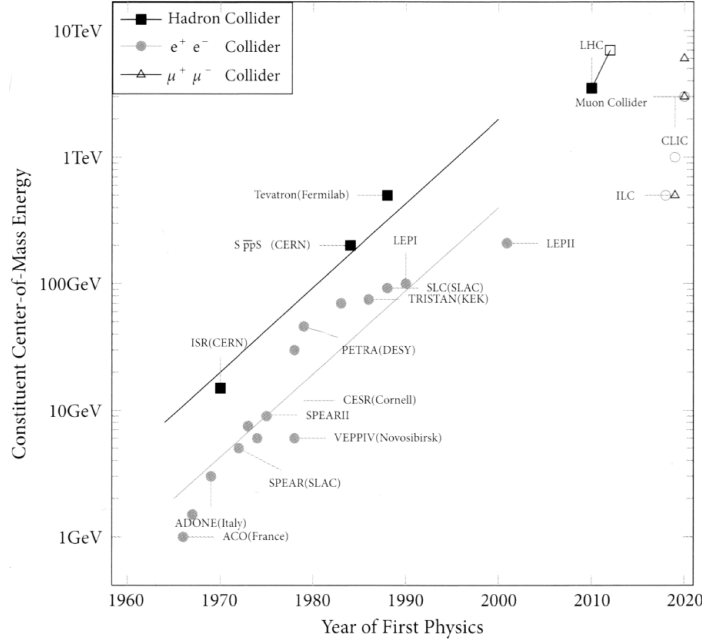


Figure 1.1: Livingston plot of the centre-of-mass collision energy for the colliding particles. From [1].

is required to ensure that the accelerator can handle unexpected situations without losing the beam inside the machine. One key component of a machine protection system is Beam Loss Monitoring (BLM), detectors placed outside of the accelerator that measures the secondary particle shower generated by lost particles. A BLM system can detect the magnitude of the losses, and trigger a beam dump if the losses exceed predefined limits, and knowledge about the magnitude and location of the losses can be used to tune the machine.

This work is about developing the BLM system at the CLIC Test Beam Line, a machine used to test key components of the CLIC acceleration scheme. By simulating different loss scenarios, the secondary particle shower at the detector locations can be estimated. Combined with the detector response, this allows for calculating the amount of beam lost in the TBL based on the detector signals. This can then be compared with measured BLM values to find the amount of beam lost.

Chapter 2 gives an introduction to Beam Loss Monitoring, detection principles and

requirements on a BLM system.

Chapter 3 gives an introduction to the Compact Linear Collider study. Key technological solutions are presented, and the requirements on a BLM system at CLIC is discussed.

In Chapter 4 an overview on the BLM technology used at the Test Beam Line is presented. Details about how the BLM detectors work, as well as performance considerations, are discussed.

Chapter 5 introduces the FLUKA model of the TBL that has been used in the simulations. Details about the simulated geometry, materials, magnetic fields, simulated detector locations and custom routines are presented.

Chapter 6 contains the results from simulations of beam losses at a single quadrupole. Losses are most likely to occur at the quadrupoles, and the installed detectors are mainly sensitive to these losses.

In chapter 7 the results of other considered loss locations are presented. The effect of these losses on the BLM system are compared to losses at a quadrupole.

Chapter 8 contains calculations of the sensitivity of the BLM detectors for the settings they have been used at. It also includes details about the simulated secondary particle shower at the detector locations, to give a value of the detector sensitivity expressed in generated signal per electron lost in the TBL.

In chapter 9 measurements done by the BLM system while the TBL is running are analysed. Using the sensitivity calculated in chapter 8, the total amount of beam loss is estimated.

Chapter 10 contains conclusions of the work.

Chapter 2

Beam Loss Monitoring

A Beam Loss Monitor (BLM) typically observe the particle shower caused by the loss of beam particles which interacts with accelerator components such as vacuum pipes or magnets. BLMs are important components of the machine protection scheme at several accelerators, as knowledge of the beam losses can be used to protect the accelerator and surrounding environment from damage. BLMs are also useful for diagnostic purposes, by finding the location and intensity of a loss.

The choice of BLM technology for an accelerator depends on the losses that can be expected. To evaluate the losses, Monte Carlo simulations are often performed, using software such as FLUKA [2] [3] or Geant4. The results from the simulations will tell which detector types are appropriate, where they should be placed and what performance can be expected. An introduction to beam loss monitors can be found in [4].

2.1 Types of losses

Most beam losses fall into one of two categories:

- Irregular, or fast losses.

Irregular beam losses are avoidable, and usually the result of a misaligned beam or faulty equipment. Examples of faults are trips in the radiofrequency cavities where the acceleration occurs, obstacles such as microparticles in the beam line or fast vacuum deterioration. These losses usually occur at a single location, and must be kept to a minimum in order to avoid damaging the accelerator. One common method to identify irregular losses is to send in a ‘pilot beam’ of reduced intensity. Only if the loss of this beam is acceptably low will a full intensity beam be sent to the accelerator.

- Regular, or slow losses.

Regular losses are usually unavoidable, and occur along the entire accelerator. The losses can be caused by, for example, beam-beam interaction, interaction with residual gas or beam instabilities. These losses must be kept low enough that activation

of nearby material does not prevent hands-on maintenance, and the losses set a time limit for how long a beam can be stored in a circular accelerator.

2.2 Detection principles

A BLM system is typically mounted outside of the accelerator vacuum chamber, and measures the secondary particle shower created by the lost particles that interact with beamline components. Ideally, the BLM should be able to measure the number of particles lost, and the signal from a BLM should be proportional to the loss. The proportionality is described by the relation

$$N = \frac{S}{\epsilon}$$

where N is the number of particles lost, S is the BLM signal and ϵ is the BLM response. Estimating the value of ϵ is difficult in general, since it depends on both the BLM hardware and the characteristics of the loss. Depending on the method of detection, BLMs are sensitive to certain types of particles, and two different BLM types can give different signals when subjected to the same radiation. Some detector types give a strong enough signal that it does not need to be amplified, while others, such as those based on photomultipliers, can have an amplification of up to 10^7 . Further, the characteristics of the secondary particle shower depends on the beam energy, loss location and the angle at which the particles impact the beam pipe, and these parameters affect the intensity of the shower at different locations. Estimating the secondary particle shower intensity at a BLM location is usually done by Monte Carlo simulations. All of this must be considered when estimating the BLM response.

BLMs detect particles through their interaction with matter, and there are several interactions that are commonly used:

- Ionization.
- Secondary electron emission.
- Fluorescent or scintillating light.
- Cherenkov light.

The detector response is usually given in units of Coulombs per dose or Coulombs per Minimum Ionizing Particle (MIP). The most commonly used BLM signal source is the ionizing capability of the charged particle shower, described by the by the Bethe formula [5]. The ionizing energy deposited by a charged particle reaches a minimum at $p/m_0c \approx 2$, and a particle at this energy is referred to as a MIP. For an electron, this occurs roughly at 1 MeV. Above this energy, the increase in energy deposition is logarithmic, and for BLM purposes, all particles with $p/m_0c \geq 2$ can be considered to be a MIP [4]. The energy deposited by a MIP is $dE/dx_{\text{MIP}} = 1 - 2 \text{ MeV}/(\text{g}/\text{cm}^2)$, which is valid for many materials. This value must be multiplied by the material density to get the energy

deposition per traversed distance by a charged particle in the material. As an example, the energy deposition various particles in several materials are shown in figure 2.1

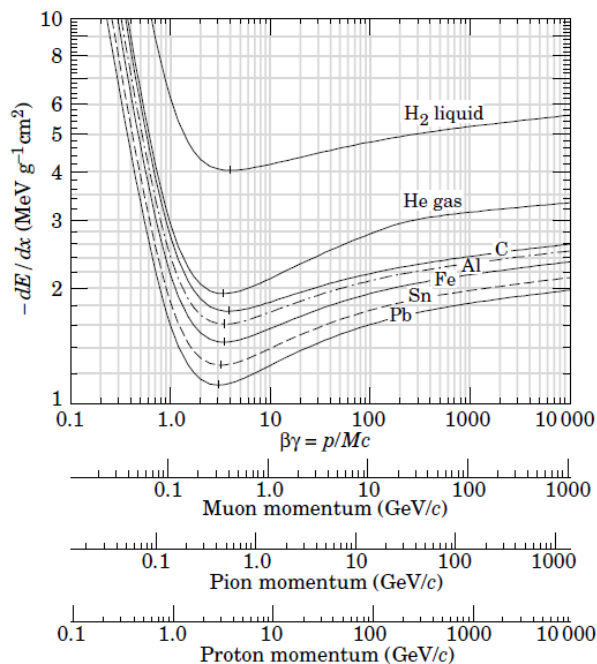


Figure 2.1: Energy deposition in several materials by muons, pions and protons. From [5].

2.3 Selecting an appropriate detector

The choice of a BLM must be done with respect to the acceptable loss level at an accelerator, at the same time considering the minimum sensitivity required for diagnostic purposes. BLM systems should preferably have a temporal and spatial resolution sufficient to characterise the losses, as well as giving the total amount of beam lost over extended periods of time. For electron accelerators, the secondary particle shower consist mainly of electrons, photons and positrons, and a BLM system should be sensitive to the constituents of the shower. Important considerations when choosing a BLM system are:

- Resolution and sensitivity.

The detectors should be fast enough to resolve the time-structure of the loss. For detectors that covers a large region, it should also be possible to resolve the location of a loss. It should have a dynamic range that covers everything from low losses to the maximum allowed losses at the accelerator. It should be sensitive to the particle types and energies expected to be present in the secondary particle shower, and be unaffected by background radiation. It should also ignore radiation that is part of normal operations and not caused by losses, such as synchrotron radiation in circular accelerators.

- Physical size.

A small detector will be easier to install and move. It will also be easier to remove the detector should it need repair or replacement.

- Calibration and maintenance.

Certain detectors need periodic calibration, since their gain can drift due to ageing or radiation damage. Some detectors can be calibrated in place, while others must be removed and calibrated in controlled conditions. From a maintenance perspective, detectors should be robust, reliable, radiation hard, easy to inspect, easy to repair or replace, and different BLM should have little individual variations in performance.

- Cost.

The cost of the detectors is not only the cost obtaining the hardware, but also for maintenance, and for the amount of other required hardware, such as signal cables and electronics. Readily-available BLMs should be preferred to custom ones.

- Output.

The output signal is usually a pulse or a current. Certain signals need to be amplified to be measured, and this can require additional hardware, power supplies and cabling.

Chapter 3

The Compact Linear Collider

The Large Hadron Collider (LHC) [6] at CERN is the most powerful particle accelerator built to date, achieving a centre-of-mass collision energy of 7-8 TeV. The LHC has been able to probe physics at a previously unexplored energy range, allowing investigation of the Standard Model (SM) as well as physics beyond the standard model, such as supersymmetry (SUSY), extra dimensions and miniature black holes. The most spectacular result delivered so far is the discovery of a new boson, now confirmed to be the long sought Higgs boson of the SM. After its first run (2010-2013), the LHC was shut down for maintenance and upgrades, and it will resume colliding protons in 2015 at 14 TeV. At this higher energy, the LHC will search further for new physics, as well as making precision measurements of the properties of the new boson.

What makes precision measurements difficult at the LHC is that it collides protons, which are not elementary particles. Protons are made from quarks and gluons, and it is impossible to know which constituents are colliding. To get better precision, one could use elementary particles such as leptons that have a well defined mass. The most powerful lepton collider built was the Large Electron-Positron collider (LEP) [7] at CERN, with a centre-of-mass energy of 209 GeV, that was housed in the tunnel now occupied by the LHC. Being a circular accelerator, the energy of LEP was limited by synchrotron radiation that is emitted when the trajectory of a charged particle is bent by a magnetic field. The energy lost in one turn due to synchrotron radiation is proportional to

$$E_{synch} \propto \frac{E^4}{Rm_0^4}$$

for a particle of rest mass m_0 and energy E in an accelerator with radius R . In LEP, each beam lost about 3% of its energy per turn, and at peak energy the acceleration provided by the machine was just enough to compensate for this energy loss. There are two proposed methods to overcome this limitation:

- Using muons instead of electrons and positrons.

Since muons have a mass that is 200 times that of an electron, the energy lost to synchrotron radiation is negligible in comparison. Feasibility studies for muon colliders are ongoing, but several challenges remain. Since muons are not stable

particles, but have a mean lifetime of 2 ms (measured in a rest frame), the muon beam needs to be produced, cooled and accelerated in a very short time interval.

- Using a linear accelerator to collide electrons and positrons.

Since the particle trajectories are straight, a linear accelerator generates very little synchrotron radiation.

The only method to get electron-positron collisions at TeV energies is to use a linear accelerator, that operates quite differently from circular accelerators. In a circular accelerator, two beams are circulating in opposite directions. Since the particles return to the same position after completing a turn, it is enough to do the actual acceleration at a single location. A linear collider is made from two linear accelerators (linacs), one accelerating electrons and the other positrons. The linacs face each other so that the particles collide head-on. The particles are accelerated in a single pass, and the linac must have a high accelerating gradient in order to keep the linear collider length reasonable.

Another difference is that in a linear collider, particles collide only once, which sets a repetition frequency of 5-100 Hz. In a circular collider, the repetition frequency is much higher, and in the LHC collisions occurred with a repetition frequency of 20 MHz. In order to get the luminosity required for particle physics experiments, a linear collider must have a small beam size at the collision point, and have a bunch charge that is as high as possible.

Currently research and development is ongoing for two technical solutions for a linear collider:

- The International Linear Collider (ILC) [8]

The ILC is based on more conventional technology, and will achieve a centre-of-mass energy of 500 GeV, with a possible upgrade to 1 TeV. It uses superconductive radiofrequency (RF) cavities for acceleration with a nominal accelerating field 31.5 MV/m, and will have a total length of 31 km. Due to fundamental limitations in the superconductive cavities, it is not possible to achieve much higher accelerating gradients.

- The Compact Linear Collider (CLIC) [9]

CLIC uses a novel two-beam scheme and normal conducting cavities to overcome the limits of superconductive cavities. It is expected to be built in stages, starting at the minimum energy of interest to physics, and can be upgraded to a total centre-of-mass energy of 3 TeV. Using normal conducting travelling-wave accelerating structures, it can achieve a nominal acceleration of 100 MV/m, and will have a total length of 48 km to operate at 3 TeV. In order to operate at this high energy, a new way of supplying power was developed, where a high-intensity drive beam provides power to the high-energy main beam [10], as shown in figure 3.1.

On the 21st February, 2013, it was announced that ILC and CLIC would merge to a single organization, the Linear Collider Collaboration (LCC) [12]. The LCC will have three main sections, one for ILC, one for CLIC, and one for physics and detectors. While research is ongoing for both ILC and CLIC, they have reached different stages of maturity. CLIC

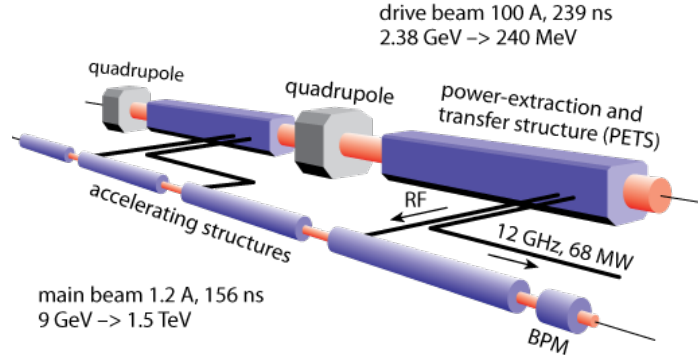


Figure 3.1: The CLIC two-beam scheme. Power is extracted from the high-power drive beam by the PETS tanks, and is transferred to the high-energy main beam. [11]

has published its Conceptual Design Report [11] in 2012, and is scheduled to complete its Technical Design Report in a few years. ILC has published a finalized version of the Technical Design Report in 2013, and is now ready for construction [13].

3.1 CLIC layout

The most important feature of the CLIC acceleration scheme is the two-beam scheme used. In the main linac, the Drive Beam (DB) and the Main Beam (MB) run in parallel, at a distance of 65 cm. There are also several structures needed to generate the beams before they are injected into the main linac. The drive beam is created by combining several beams of lower intensity, and the main beam must be cooled before it can be accelerated, to keep the beam size small. Transfer lines to transport the beams from the injectors to the main linac can be housed in the same tunnel, under the ceiling. Figure 3.2 shows a schematic of the proposed CLIC layout.

3.1.1 Drive Beam

The drive beam is created and accelerated to 2.4 GeV by the drive beam accelerator. To generate the 100 A drive beam, 24 beams of 4 A from the drive beam accelerator are combined. The first combination is done by a delay loop with combination factor 2, followed by two combiner rings (CR1 and CR2) with combination factor 3 and 4, giving a total combination factor of 24. After the combination, the drive beam is delivered to one of the decelerator sectors in the main linac.

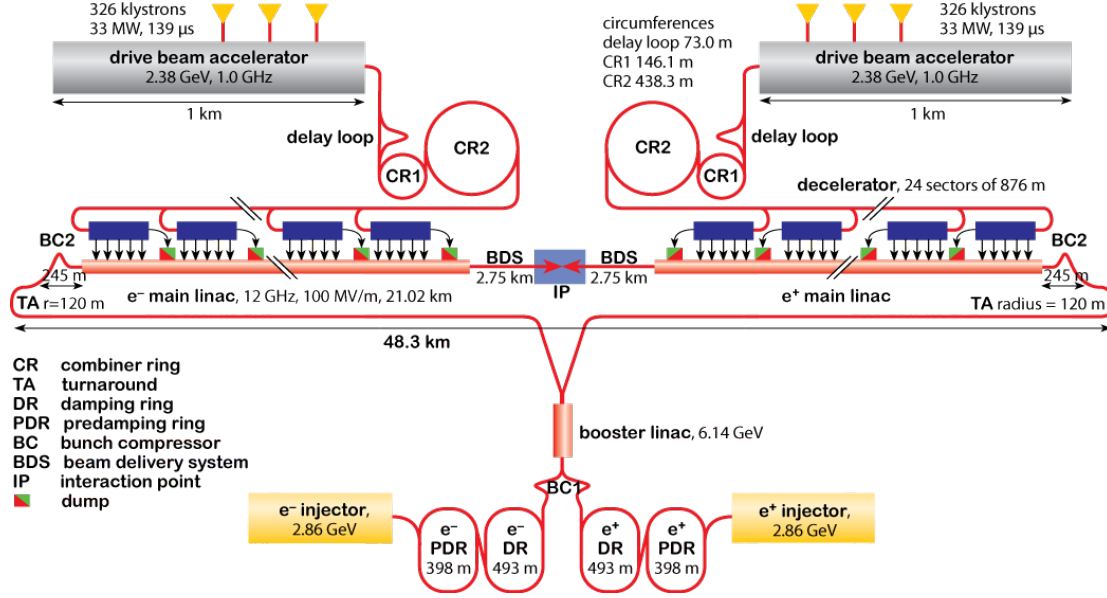


Figure 3.2: The proposed CLIC Layout. [11]

3.1.2 Main Beam

The electron and positron beam originate from two injectors, that give the beams an initial energy of 2.8 GeV. In order to obtain the high luminosity required, the beams must have a very low emittance. This is achieved by cooling the beams in a pre-dampening ring (PDR) and a dampening ring (DR). The beams are further accelerated by a booster linac, before being delivered to the main linac. Immediately before the interaction point, a Beam Delivery System (BDS) focuses the beam to a rms size of 1 nm in the vertical plane and 40 nm horizontally.

3.1.3 Main linac

The main linac is made from modules, called Two Beam Modules (TBM), shown in figure 3.3. For the drive beam, each module contains up to four Power Extraction Transfer Structures (PETS) tanks and two magnetic quadrupoles to focus the beams. The PETS tanks extract power from the drive beam by converting the kinetic energy of the beam to radiofrequency (RF) power, with about 84% efficiency. The RF power is extracted via a waveguide leading to a main beam Accelerating Structures (AS), and each PETS tank

powers two AS. The main beam module consists of up to eight AS, and a quadrupole when necessary. To make room for the MB quadrupoles of different lengths, AS must be removed, together with the PETS tank powering them. A total of five different modules exists, allowing for varying quadrupole lengths in the MB. Module Type-0 has no quadrupole and all eight AS present, while Type-1 to Type-4 has a quadrupole, replacing 2-8 AS. Each module is 2010 mm long, and the main linac is made from more than 10 000 modules.

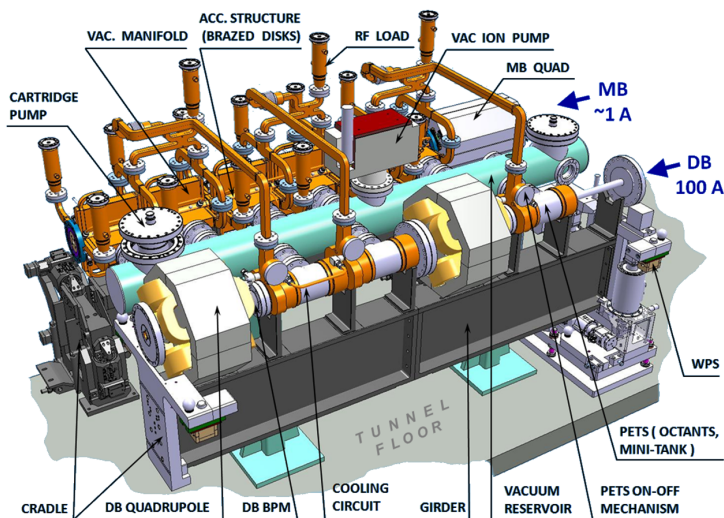


Figure 3.3: CLIC two beam module. [11]

3.1.4 Detectors

The two detectors proposed for CLIC are based on designs for the ILC detectors, the International Large Detector (ILD) and Silicon Detector (SiD). Since there is only one interaction point, the detectors will be moved several times per year using a so-called ‘push-pull’ system. By having two detectors, the results found by one detector can be verified by the other one.

3.2 Machine protection at CLIC

With a main beam of 14 MW and a drive beam of 70 MW, losses of only a fraction of a beam in CLIC can have severe consequences. The different kind of failures can be divided into three broad categories:

- Fast failures.

Fast failures occur while beam is passing through the accelerator. For early failures, the BLM system can detect these from the losses and trigger a beam dump, but for failures in the main linac it is too late to abort the beam. Typical examples are kicker magnet misfirings or malfunctions in the klystrons providing the accelerating power. Each of these can cause the beam to change trajectory, making it hit some part of the accelerator.

- Failures between cycles.

If any equipment fails in-between acceleration cycles, it can usually be detected and subsequent injections can be stopped. These failures can typically be power supply failures, positioning failures, or vacuum failures.

- Slow failures.

Slow failures develop on timescales longer than the accelerator repetition frequency, and can cause a slow increase in losses. This can be caused by, for example, temperature drifts or saturation effects. Normally the beam feedback system will detect such changes and compensate accordingly.

One important machine protection strategy at CLIC is the next cycle permit. After every cycle, the permit is revoked, and only after the accelerator has passed a number of self-tests will the permit be reinstated. Every machine component has about 8 ms between each cycle to perform these checks. Some important parameters for CLIC are summarized in table 3.1.

Parameter	Symbol	Main Beam	Drive Beam
Particle energy	E	9 - 1500 GeV	0.24 - 2.4 GeV
Particles per bunch	k_b	$3.72 \cdot 10^9$	$5.25 \cdot 10^{10}$
Bunches per train	N_b	312	2928
Bunch separation	δt_b	0.5 ns	0.083 ns
Train length	τ_t	156 ns (45.6 m)	244 ns (73.2 m)
Beam power	P_b	14 MW	70 MW

Table 3.1: Parameters for CLIC.

3.3 BLM requirements at CLIC

The BLM system is an important part of the machine protection scheme at CLIC. Its main purpose is to detect dangerous losses in the accelerator, and prevent subsequent injection of the main beam and the drive beam into the main linac, should the losses be too great. In the main linac, losses in the high-power DB or in the high-energy MB can have catastrophic consequences. A secondary task for the BLM is to provide diagnostic information. By

analysing the losses and finding the origin, important information is gained about the status of the machine, which allows the operators to optimize its performance. A thorough study of the CLIC BLM requirements can be found in the CLIC Conceptual Design Report (CDR) [11].

3.3.1 Sensitivity and dynamic range

The BLM systems must be able to detect a wide range of losses, from standard operational losses, such as beam-gas interactions, to dangerous losses, such as if a portion of the beam hits an aperture restriction. For most of the accelerator, losses should be kept at less than 1 W/m. For the main linac, losses greater than 10^{-3} will result in a lowered luminosity. To detect the onset of such losses, the sensitivity is specified with respect to the signal obtained for a loss of a factor 10 less. These requirements set a lower limit for the dynamic range [14].

The CLIC main beam is accelerated from 9 to 1500 GeV in the linac, and the drive beam is decelerated from an initial energy of 2.4 GeV to an energy of approximately 0.24 GeV. The BLM system must be able to detect losses caused by particles of all these energies, and the upper detection limit is for destructive losses, that can damage parts of the accelerator. Destructive losses occur when approximately 1% of the DB or 0.01% of the MB is lost. To limit the dynamic range of the BLMs, the upper detection limit can be set to 10% of the resulting signal of a destructive loss [11]. Simulations have been run with FLUKA to estimate the dose near the accelerator at destructive losses, and based on the results an estimate of the dynamic range of 10^6 is obtained.

3.3.2 Temporal and spatial resolution

The machine protection used at CLIC is based on a ‘next cycle permit’ scheme, where the permit is revoked after each cycle and renewed when the machine has passed several beam and equipment checks. With a repetition rate of 100 Hz, the BLM systems are required to take data and process it in less than 8 ms. For diagnostic purposes, a time resolution of a few ns is required to resolve the loss pattern of a bunch train.

The DB and MB are separated by 65 cm, so the horizontal spatial resolution should therefore be better than this, in order to be able to distinguish losses from the two beams. This effect, that losses from one beam will be measurable in detectors that monitor the other beam is referred to as ‘cross-talk’. The characteristics of the DB and MB are quite different, the DB being a high-current low-energy, and the MB being high-energy low-current. The different time characteristics of the two beams may also be used to distinguish the source of the losses. The MB and DB has bunch trains that are 156 ns and 244 ns respectively, and the DB starts 88 ns earlier than the MB.

For the longitudinal resolution, losses are expected at quadrupoles that are 1 m apart where they are the closest in the DB, so a resolution of 1 m is desirable.

3.3.3 Life time and radiation hardness

The CLIC BLM system will operate in a radiation intense environment, where the total absorbed dose near the beam line has been estimated to 10^5 Gy/year [15]. Ideally, the BLM equipment should have a sufficient radiation hardness to operate for the entire accelerator lifetime. The gain of a detector will generally change after irradiation, resulting in the need for periodic calibration. The change in gain must be slow enough that the detector gives reliable output in between calibrations.

3.3.4 BLMs considered for CLIC

The baseline choice of BLM technology is an ionization chamber, similar to the type used at LHC. The only exception is at the pre-dampening and dampening ring, where a Cherenkov radiator coupled to a photomultiplier is the baseline choice. The ionization chamber by itself has an excellent dynamic range, but it is limited by read-out electronics to 10^5 . Development of the electronics is ongoing, to increase the dynamic range to 10^6 . This will allow the detector to measure everything from low operational losses to destructive losses. In total, more than 50 000 BLM detectors of these types will be needed, the majority at the main linac. This number can be greatly reduced by halving the number of ionization chambers at the DB, by placing them only after every two quadrupoles.

Other BLM types are also under investigation, such as diamond detectors, Cherenkov fibers and long ionization chambers. Diamond detectors are interesting since they are radiation hard and have a low leakage current. Cherenkov fibers and long ionization chambers both have the advantage that they are spanned along the accelerator, and can cover up to 100 m using a single detector. Using these technologies the total number of detectors can be greatly reduced. Cherenkov fibers have been shown to give a good spatial resolution, down to 12 cm for single bunch losses [16]. The spatial resolution of a long ionization chamber has yet to be investigated.

3.4 CLIC Test Facility

The CLIC Test Facility (CTF3) [17] was built to test key technological components for CLIC, and to prove that the two-beam acceleration scheme is feasible. It consists of an 150 MeV linac followed by a delay loop and a combiner ring with combination factors 2 and 4 respectively. The beam is then sent into the CLIC EXperimental area (CLEX), and is either sent to the Test Beam Line (TBL) or the Two Beam Test Stand (TBTS). CTF3 also allow a unique opportunity to test other equipment at conditions similar to CLIC, such as the BLM system.

3.4.1 Two Beam Test Stand

At the Two Beam Test Stand the acceleration scheme is tested. A probe beam is generated by a linac called CALIFES in the CLEX hall, and is sent to a TBM module, consisting of

a PETS tank and an AS. The CTF3 drive beam is led to the PETS tank to generate RF power that is transferred to the AS, which accelerates the probe beam.

3.4.2 Test Beam Line

In CLIC the drive beam will be decelerated from an initial energy of 2.4 GeV to an energy of approximately 0.24 GeV, and the purpose of the TBL is study the characteristics of the drive beam under deceleration albeit at lower energies. The TBL consists of 16 modules, each containing a quadrupole, a Beam Position Monitor (BPM) and a PETS tank. Four of the PETS tanks have not yet been installed, in the first and in the last three modules. A comparison of the CLIC and TBL parameters can be found in table 3.2.

Parameter	Symbol	TBL	CLIC
Number of PETS	N_{PETS}	16	1492
Length of PETS [m]	L_{PETS}	0.80	0.21
Number of FODO cells	N_{FODO}	8	524
Length of FODO cells [m]	L_{FODO}	2.82	2.01
Initial energy [MeV]	E_0	150	2400
Initial average current [A]	I_0	28	101
Power per PETS [MW]	P	138	135
Mean energy extracted [%]	η_{extr}	54	84
PETS sync. freq. [GHz]	f_{rf}	12	12
Pulse length [ns]	t_{pulse}	140	240
Transient length [ns]	t_{fill}	3	1
Bunch rms length [mm]	σ_z	1.0	1.0
Init. norm. emittance [μm]	$\epsilon_{Nx,y}$	150	150
Beam pipe radius [mm]	a_0	11.5	11.5

Table 3.2: Different parameters at TBL and CLIC. [18]

Chapter 4

BLM equipment at CTF3

The BLMs installed at CTF-3 TBL includes several localised detectors and a Cherenkov fiber BLM. The main aim of the localised detector BLMs is to provide information on losses for the CTF-3 operation. While the fiber is not an ideal technology choice for measuring TBL losses, the main aim for the installation of the fiber is to test its suitability for CLIC, where cost consideration is a more important factor.

There are 16 quadrupoles in the TBL, and throughout this report the quadrupoles will be numbered by their position in the TBL. The most upstream quadrupole at the beginning of the TBL will be the first quadrupole, and the most downstream one will be the 16th quadrupole.

4.1 Installed equipment

The BLM detectors currently installed at CTF3 TBL consist of eight Aluminium Cathode Electron Multiplier (ACEM), a detector borrowed from the PEP-II accelerator and a diamond detector, which are all localized detectors, as well as a Cherenkov fiber. The ACEMs are installed after quadrupoles 3,4,7,8,11,12,15 and 16, so that every other quadrupole pair is covered. The PEP-II and the diamond detector are installed after quadrupole 8 so that the performance of all three localized detector types can be compared under the same conditions. The Cherenkov fiber was originally installed running along the TBL in a cable tray at a distance of about 1 m from the beam line. The fiber was later moved closer, to a distance of 28 cm from the beam line.

There is also other equipment installed in CTF3 that can be used to estimate the beam losses and beam conditions, such as Beam Position Monitors (BPM) and Radiation Monitors (RADMON).

4.1.1 ACEM

An Aluminium Cathode Electron Multiplier (ACEM) is a photomultiplier where the cathode has been replaced by a thin aluminium foil. This makes the detector sensitive to charged particles, rather than the optical photons that a photomultiplier is normally sensitive to. When incident radiation strikes the cathode, electrons are created by secondary

emission, that are led to a series of electron multipliers, or dynodes, as shown in figure 4.1. The dynodes are given a potential, so that a ‘potential ladder’ is set up. Electrons from the cathode will be accelerated to the first dynode, and when they impact many more secondary emission electrons are created, that are subsequently drawn to the next dynode. This is repeated through the dynode ladder, until the electrons finally reach the anode. Since a single incident electron can create several secondary emission electrons, the electron pulse will be greatly amplified when passing through the dynodes. Most commercial photomultipliers contains 10-14 dynode stages, and can have a total gain of up to 10^7 [19].

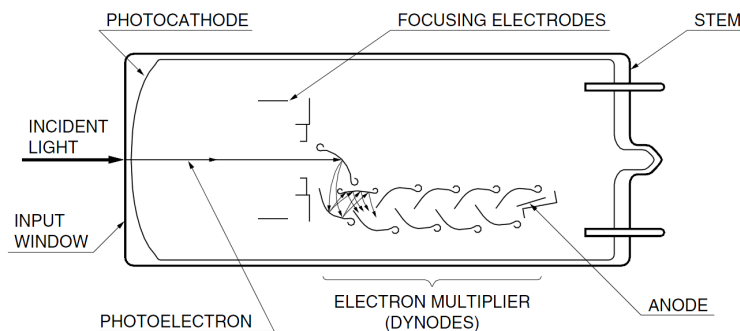


Figure 4.1: Schematic of a photomultiplier tube. From [20].

ACEMs have previously been installed at the Proton Synchrotron and at the Booster at CERN. Thanks to a fast signal rise-time, of typically < 10 ns, these detectors can measure the losses of individual bunches at these accelerators [21]. At CLIC, the main beam consists of bunches separated by 0.5 ns, and 314 bunches form a bunch train. In the drive beam, a bunch train is 244 ns and consists of 2922 bunches. The ACEM detectors are not fast enough to measure losses from individual bunches, but they are fast enough to distinguish losses within a bunch train.

Because of ageing due to radiation, the gain of an ACEM will vary throughout its lifetime, and it must be calibrated periodically. The gain will also be affected if the detector is placed in a strong magnetic field. Since losses are expected after magnetic quadrupoles in the TBL, the detectors are placed just after the magnets, but the magnetic fields there are small enough to not affect the gain significantly. Shielding the detector using several layers of a metal with high magnetic permeability will allow it to operate normally at fields up to 200 Gauss [22].

The ACEMs installed at CTF3 TBL were purchased from Hamamatsu, and are no longer being sold, and other detectors are considered for replacing the ACEMs.

4.1.2 PEP-II

The PEP-II detector was developed for use at the PEP-II accelerator at Stanford, and several of these detectors have been borrowed by CERN. The detector is a small Cherenkov detector, made from a fused-silica Cherenkov radiator, coupled to a photomultiplier tube. When charged particles with sufficient velocity enters the radiator, Cherenkov radiation is produced. The radiator is covered in a reflective material, so that the radiation is directed towards the photomultiplier. Like the ACEM, the PEP-II is a fast detector, generating signal pulses with a width of a few ns [23]. Since the PEP-II is sensitive to Cherenkov radiation, it will not detect low-energy particles or neutral particles, such as photons generated by the beam losses.

4.1.3 Diamond detector

Diamond is one of the most radiation hard materials known, which makes it well suited to work as a detector in environments with extreme radiation. Diamond detectors have been installed in the CERN experiments ALICE, ATLAS, CMS and LHCb, as well as in several particle physics laboratories in USA and Japan. Both ATLAS and CMS are considering to upgrade the innermost tracker layer to a diamond detector during the LHC long shutdown. Much research has been done in investigating the properties of diamond, for example by the RD42 Collaboration, and the production technology has matured to the level that these detectors can be bought commercially [24].

A diamond detector works as a solid state ionization chamber. Contacts are applied to the opposite ends of a diamond film, and a bias voltage is applied. When particles pass through the diamond, they lose energy, and can promote a valence band electron into the conduction band, leaving behind a hole. Because of the bias voltage, the electrons and holes will propagate through the detector, and can be collected and measured when they reach the edges.

The diamonds are created by a Chemical Vapour Deposition (CVD) process. Precursor gases, normally H_2 and CH_4 , are first sent into an activation stage, where high temperature or electric discharges causes these molecules to fragment into reactive radicals. The carbon is then deposited onto a substrate, where it can bond to other deposited carbon atoms. Any free H atoms will try to etch at these bonds, and will etch sp^2 graphite bonds much faster than sp^3 diamond bonds, resulting in a slow growth where only diamond remain.

Types of diamond detectors There are two main types of diamond detectors that have been studied for usage in particle physics, polycrystalline CVD (pCVD) diamonds and single crystal CVD (sCVD). The pCVD diamond is grown on a substrate, where diamond crystal grains of different sizes are formed. Grains that are larger tend to grow faster, leading to that the small grains stop growing, and that the grains become fewer and larger as the diamond grows. The bottom layer, with many small grains, is usually removed by resin polishing or ion etching, leaving a diamond with as few grain boundaries as possible. The sCVD diamond is grown on a high-pressure high-temperature diamond lattice, resulting in a perfect lattice match. This allows the crystal to grow as a single

grain, with no grain boundaries inside the material.

For optimal detector performance, the number of impurities and defects in the crystal should be kept at a minimum, thus sCVD diamonds outperform pCVD diamonds. Growing sCVD diamonds is however more complicated, and pCVD diamonds are cheaper and available in larger sizes.

Properties The bandgap of diamond is 5.5 eV, making it a large bandgap semiconductor or even an insulator. Due to the large bandgap, the number of electron/hole pairs is negligible at room temperature, giving diamond detectors a low dark current. Diamond also has a thermal conductivity of $25 \text{ W cm}^{-1} \text{ K}^{-1}$ at room temperature, six times higher than copper. These effects allow for the usage of diamond at room temperature without any cooling, even in high-intensity radiation.

The cohesive energy in diamond is 3.62 eV/bond, and the radiation hardness of diamond comes from the high strength of the bonds. Sample detectors have been found to be operating after being absorbing a dose-equivalent of 7 MGy of relativistic electrons [25]. At CLIC, the total dose is expected to be 10^5 Gy/year near the beam line, so diamond detectors can survive operating during the entire accelerator lifetime. The detector response will change with the absorbed dose, so periodical calibration of the detectors is still necessary. The effect of the radiation damage is the same for both sCVD and pCVD diamond, and pCVD behaves as sCVD that has already been damaged.

Sensitivity Diamond is sensitive to a wide range of particles, such as protons, electrons, neutrons, and photons, but is mainly sensitive to charged particles. When a charged particle pass through the diamond, it will ionize the atoms in the detector, promoting valence band electrons into the conduction band. On average, 36 electron/hole pairs are created per μm of diamond traversed by a minimum ionizing particle (MIP). For neutrons, the main interaction is elastic and inelastic reactions, which can also generate electron/hole pairs.

Diamond is also sensitive to photons of certain energies. For energies less than 100 keV, photons mainly interact via the photoelectric effect. For energies between 100 keV and 2 MeV interactions occur mainly through Compton and Rayleigh scattering. For energies above twice the rest energy of an electron-positron pair (1.02 MeV), pair production becomes the dominant form of interaction. Because of the high band gap, diamond is transparent to visible light, so no shielding is required to remove background light. Diamond is also highly transparent to X-rays and γ -rays, thus it can be used in locations where there is an intense background radiation, such as synchrotrons or nuclear reactors [26].

4.1.4 Cherenkov fiber

The Cherenkov fiber detector is a fiber-optical cable running alongside the accelerator. When charged particles pass through the fiber with a velocity greater than the phase velocity in the fiber material, Cherenkov radiation is generated. These photons are emitted

on a cone, with the angle to the particle trajectory θ_c given by

$$\cos \theta_c = \frac{1}{n\beta}$$

with n being the refractive index of the medium and $\beta = v/c$. For certain particle velocities and incident angles with respect to the fiber, the photons will be trapped in the fiber due to total internal reflection, and will propagate to the fiber ends. There they can be detected using a photomultiplier.

While the Cherenkov fibers are not localized detectors, they can still give a good time and space resolution of the losses. For losses at a single point, the timing of the fiber signal will give the position of the loss to within 1 m, assuming that the signal pulse is short, on the order of a few ns [27]. For losses at multiple locations, longitudinal resolution is much more problematic. The resulting signal can however be used to estimate the total loss along the detector, which is also important for machine protection.

Due to attenuation in the fiber, the detector can not be much longer than about 100 m. For CLIC, the main two linac stages are 42 km, so several hundred Cherenkov fibers will be needed to cover the accelerator. For localized detectors, it is estimated that around 45 500 detectors will be required [11]. This makes the fibers an attractive solution for BLM, since it is commercial technology and thus cheaper, less readout electronics will be required, and it may still be possible to determine the location of the losses with good resolution. Further advantages of fiber detectors are that they are not sensitive to magnetic fields or to changes in temperature, which simplifies their installation and usage.

The quartz in the fiber is radiation hard, although radiation induced attenuation (RIA) does occur, which limits the lifetime of the detector. It is not known if the radiation levels in CLIC will be so high that the fibers require periodic replacement, or if they can survive for the entire accelerator lifetime.

To detect the photons exiting the fiber, a custom detector box has been constructed, and is under development at CERN. It consists of a Multi Pixel Photon Counter (MPPC) connected to a current-to-voltage converter. The MPPC is a semiconductor photon detector, with a detection area consisting of pixels that are Avalanche Photo-Diodes (APD). When a photon strikes the APD, an electron-hole pair is formed, that is accelerated by an applied voltage. If this voltage is high enough, the electron gets enough energy that it can generate additional electron-hole pairs, that are subsequently accelerated. The initial electron-hole pair thus create an avalanche of charges, and an electric signal can be measured. Each APD also has a quenching resistor, that ensures that the avalanche is eventually stopped, and the output signal is thus a pulse.

The APD pixels are connected, and the output is the sum of each APD signal. An MPPC has good linearity, but if a second photon creates an electron-hole pair while an avalanche is occurring, it will not create a separate avalanche, and not be detected. After the avalanche is quenched, the APD requires some time to recharge, and if a photon is detected before the recharge is complete, the resulting current pulse will have a lower amplitude. In general, an MPPC becomes saturated when about 30 % of the APD are active at a time.

4.1.5 Installation at CTF-3

The localized detectors are mounted on a metal rod that has been attached to the support girder that the TBL is mounted on. The height of the detector and the direction at which it is facing can be changed. Several different heights have been tried under varying beam conditions, and the detectors were always installed facing the centre of the quadrupole. The Cherenkov fiber was initially installed in a cable tray running parallel to the TBL, at about 1 m distance from the beam line. Since preliminary data and simulations suggested that the signal was very low, and drowned in the background signal, the fiber was later moved closer to the beam line. A rope was installed running 28 cm above the beam line, and the fiber was attached to the rope, to prevent it from sagging too much.

Power to the localized detectors is provided by a power supply located in the gallery above the experimental area, by high-voltage cables that run between those two areas. There is also a signal cable for each detector running between the areas, since the A/D converter that measures the signal is located in the gallery. The reason for putting the voltage supplies in the gallery is to allow for changing the voltages without having to access the experimental area.

Additional fiber-optical cables are used to take the signal from the Cherenkov fiber to the Multi Pixel Photon Counters (MPPC) in the gallery that measures the signal. Since Cherenkov photons can be generated in these fibers as well, two additional fibers run in parallel to the signal-carrying fibers. The idea is that the same background signal will be generated on these additional fibers, and the background signal can be measured from these fibers. The background signal can then be subtracted from the signal measured by the TBL fiber. This way, the resulting signal with background removed is only due to losses at the TBL. Since there are several settings that can be changed to optimize the fiber detector performance, such as voltages and distance between the fiber end and the MPPC, the detector equipment is placed in the gallery where it can be accessed easily.

4.2 Other proposed detectors

4.2.1 Ionization chambers

The ionization chamber is the baseline technology choice for BLMs at CLIC [11]. More than 4000 of these detectors were manufactured for LHC [28], so the technology is well tested. The detector consists of aluminium electrode plates in a chamber filled with nitrogen. Radiation can ionize the nitrogen, and the electrodes will collect the electrons and ions to create a current pulse. The ionization chambers are robust against ageing, and they are fast enough to be used at LHC, but they are too slow for the TBL. The charge collection time is about 300 ns for the electrons and 80 μ s for the ions. The train length at CLIC and CTF-3 is in the same order as the electron charge collection time, so the ionization chambers can be used to measure the losses from a train, but not resolve the loss structure within a train. For this reason ionization chambers are not used at CTF-3, although there are considerations to install one for benchmarking purposes.

Another type of ionization chamber is the Panofsky Long Ionization Chamber (PLIC),

which is essentially a coaxial cable filled with a gas [29]. Like the Cherenkov fibers, they can be run alongside an accelerator and cover long distances of the beam line. The time resolution of a PLIC is on the order of several μs , which is much too slow for any longitudinal resolution. However, since a single PLIC can cover an even longer distance than a Cherenkov fiber, it is an ideal technology for measuring the integrated loss along the accelerator.

4.3 Other equipment of interest

4.3.1 BPM

A Beam Position Monitor (BPM) consists of two pairs of parallel metal plates, one pair placed horizontally and one vertically. Since the beam has an electric charge, it will attract charges of the opposite sign in these plates when the beam passes in between them. This charge can be measured and used to obtain information about the beam. The charge difference can be used to obtain the position of the beam, and the charge sum can be used to obtain the total charge in the beam [30].

In the TBL, a BPM is installed after every quadrupole. By measuring the total charge at each BPM, it is possible to find how much of the beam has been lost in between the BPMs. This can be compared with the BLM signals, to see that both systems detect the same losses. The BPM system is however not as precise as the BLM system, and it is left to the BLM system to pinpoint the location and magnitude of any losses.

4.3.2 RADMON

The RADMON probe installed at CTF-3 measures the absorbed dose using radiation sensitive electronics. Since it is intended for long-term dose measurements, it is not fast enough to be used for BLM purposes. The dose measured by the RADMON can however be compared with FLUKA simulations, to see that they are consistent. It can also be compared to the total loss over long periods measured by the BLM system.

Chapter 5

FLUKA model

To estimate the BLM response for various detector locations and beam loss scenarios, simulations were done using the program FLUKA [2] [3]. FLUKA is a Monte-Carlo particle transport code, that uses modern and accurate physical models to simulate particle interaction with matter. Thanks to third-party programs such as flair [31], that provides a user-friendly interface to FLUKA, it is easy to set up a working model.

FLUKA uses Constructive Solid Geometry (CSG) to set up the geometry to be simulated. Each region specified in the simulation is given a material, with most of the important material parameters already present. While most of the standard physics parameters in FLUKA are valid for most situations, the user can modify these when necessary. Also included are several routines for measuring the simulated particles, usually referred to in FLUKA as scoring. FLUKA also allows users to write custom routines in FORTRAN to handle user-specific cases that the standard routines cannot handle, such as adding magnetic fields based on analytical fields or field maps, or starting the initial particles at specific locations.

The geometry of the TBL components in the developed model is based on technical drawings found in the CERN EDMS (Engineering & Equipment Data Management Service) database. A graphical representation of the model is shown in figure 5.1.

5.1 TBL module

The main section of the TBL consists of 16 modules, each containing a quadrupole, a Beam Position Monitor (BPM), and a PETS tank as shown in figure 5.2(a). The FLUKA model includes a detailed representation of the TBL lattice including PETS, quadrupoles, BPMs and support girder. The quadrupole was modelled in detail with an iron yoke and poles, copper coils and a stainless steel beam pipe though the center, as shown in figure 5.2(b). The PETS was modelled as hollow copper cylinders with an internal diameter of 13.5 mm and external diameter of 48 mm. A stainless steel PETS tank was also included. The BPM was modelled as a small cylinder in between the quadrupole and PETS tank. A BPM is made mainly from copper and iron, and the BPM in the simulations was given a material consisting of equal parts of these two elements.

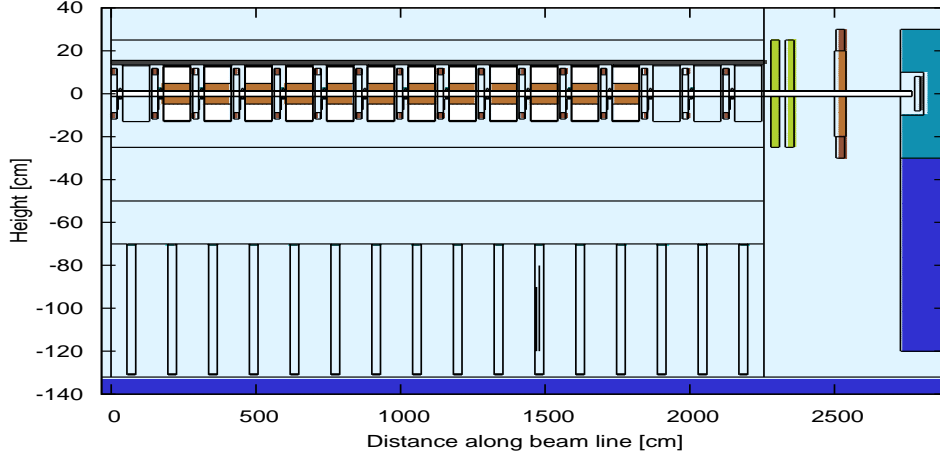


Figure 5.1: FLUKA model of the TBL used in the simulations.

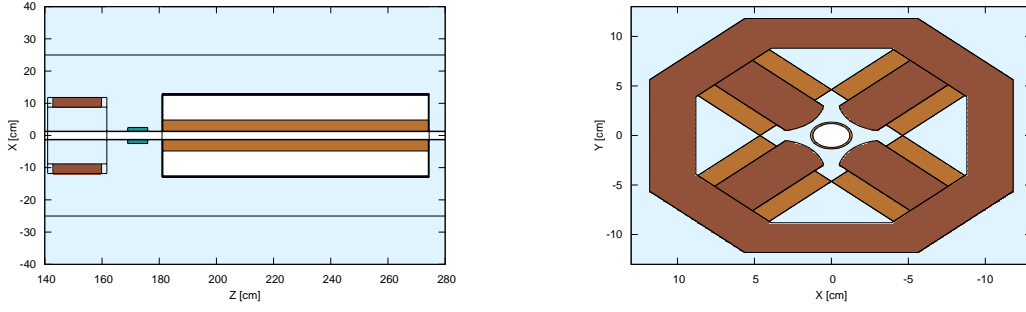
5.2 Quadrupole magnetic field

The TBL model includes a magnetic field at the quadrupoles. The field is based on a simulation done by Davide Tomassini, and was converted to FLUKA input format. For many applications, where the beam dynamics is of importance, a magnetic field map does not give sufficient resolution that the correct value can be interpolated from data. The central parts of the magnetic fields are often calculated for these parts based on a perfect quadrupole field, that scales with $1/R$. Outside of the central parts the field is interpolated from data, since the field will depend on the magnet geometry, and not be a perfect quadrupole.

In the model used, the field is analytical inside the beam pipe and uses a field map outside of it. However, for beam loss simulations, the interest is in the particles that hit the beam pipe and exit the vacuum chamber, so only the field map needs to be considered. The stray magnetic field that extends outside of the magnet is not modelled, and is expected to be weak enough to not affect the loss showers significantly and can thus be neglected. The intensity of the magnetic field inside the quadrupole is shown in figure 5.3. The intensity of the magnetic field at the TBL quadrupoles is 7.4 T/m.

5.3 Other TBL components

Although the cases of interest for a BLM system are losses at the main TBL modules, other components are also included in the model. Downstream of the TBL lattice components such as a dipole, two quadrupoles and the beam dump are included in the model. These beam line components are not modelled with the same level of detail as the main TBL



(a) TBL module with quadrupole, BPM and PETS.

(b) Quadrupole model.

Figure 5.2: FLUKA models used in the simulations.

components. The CLEX walls, ceiling and floor were included and modelled using portland concrete. The other beamlines in the CLEX hall were not included in the FLUKA model.

5.4 Regions for measuring particle showers

The regions used to estimate the fluence of particles are thin cylinders of radius 1 cm, placed 3 cm downstream of the quadrupole where the losses are simulated, and with the cylindrical axis pointing towards the center of the quadrupole. The location of the regions where the estimates of the particle shower are made are shown in figure 5.4. Regions 1a and 2 to 8 are used to investigate dependence of the showers on various loss scenarios, whereas regions 1a to 1d correspond approximately to possible locations where the detectors can be installed at the TBL.

Three cylindrical regions of radius 1 cm that run parallel to the beam line corresponding to possible Cherenkov fiber locations are also included in the model. One is 28 cm above the beam line, which is the closest that a fiber can be installed at the TBL using the current support system. One is 50 cm to the side and 70 cm above, where there is a cable tray in the CLEX hall. The third region is 1 m to the side, close to the CLEX wall. Shower particles entering these regions are usually saved to a file and analysed using a separate matlab script.

5.5 Twostep method

To improve the CPU efficiency of the simulations, a two-step method based on the MG-Draw routine developed by Chris Theis was used. In the first step, whenever a particle enters a specified region, its type, position, energy, movement direction and lifetime is saved to file, and the particle is then not simulated further. The saved data can be used

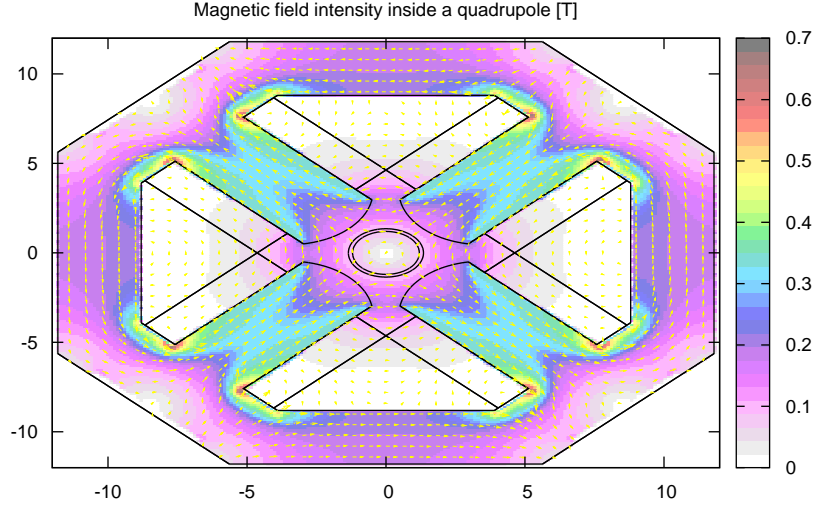


Figure 5.3: The magnetic field inside the quadrupole.

as a source for the second step. The idea is to run a long first step, and only save particles of interest, such as those entering detector regions. Several second steps can then be run with different parameters, without having to simulate particles that does not enter the detector regions and thus does not affect the results. The data files can also be analysed separately, which is how the signal from the Cherekov fiber is calculated.

5.6 Primary electron starting position

Two different loss cases have been considered in all the simulations that were done, either losses at a single location or losses distributed along the TBL. For losses at single locations, the FLUKA standard source routines are sufficient, but for distributed losses a source routine was developed to distribute the lost electrons along the TBL. The routine allows for the starting particles to be distributed evenly between the 16 quadrupoles, or to use a user-specified probability distribution to define the probability that a particle starts at each quadrupole. The particles can either be distributed evenly on the beam pipe, or only occur in a given plane that alternates between the quadrupoles, following the FODO lattice. The impact angle between the particles and the beam pipe can also be specified. The time structure of the losses is relevant, particularly in the case of the Cherenkov fiber signal. To see the effect of the beam train passing through the TBL on the Cherenkov fiber signal, each particle is given a random position in the time structure of the train, when the user has specified the length of the train. The particle is given a starting time depending on which quadrupole it starts from and where in the train it is situated.

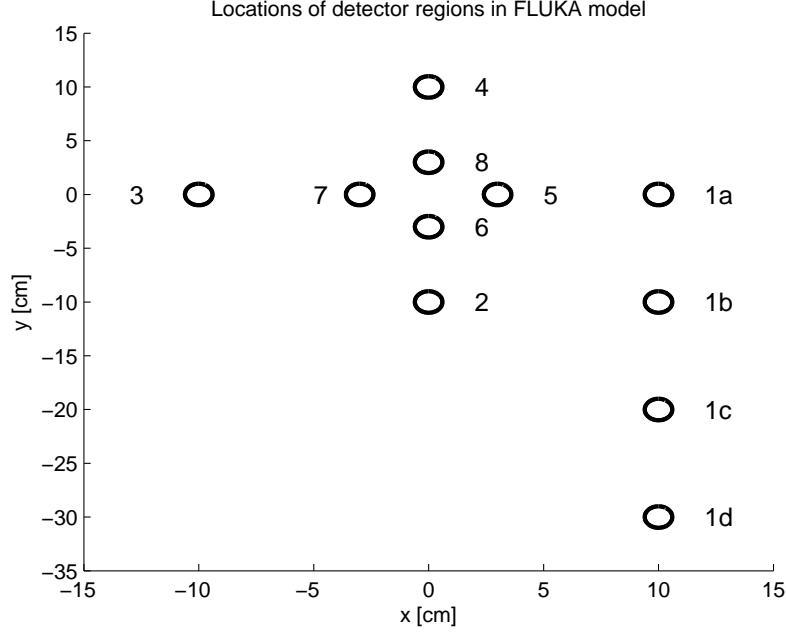


Figure 5.4: Regions downstream of the fifth quadrupole used to measure the fluence of shower particles. The center of the beam pipe is at the origin, and the plot is shown looking upstream.

5.7 FLUKA physics settings

The production and transport thresholds were set to 0.1 MeV for electrons and gammas respectively. Particles with energy below this limit are not created, and when a particle has lost enough energy to be below this limit, all remaining energy is quickly deposited and the particle is not simulated further. The transport of electrons, positrons and photons were activated, and photo-nuclear and muon-photon interactions were also activated.

Chapter 6

Simulated losses at quadrupoles

Since the response of a BLM to a loss varies with detector location, settings, and the characteristics of the loss, these must all be investigated, usually through Monte Carlo simulations. The most significant losses at the TBL are expected to occur at the quadrupoles, since the beam size is greatest there. For this reason, much effort has been put into characterising the secondary particle shower resulting from a loss at a quadrupole. As a standard loss case for the simulations, the beam has been simulated impacting the beam pipe at the longitudinal centre of a quadrupole. This is sufficient for estimating the effect of beam energy, impact angle and position in the secondary particle showers. More complicated loss scenarios are only required for estimating the BLM signal.

To be able to compare the results from the simulations, all are normalized to a single starting electron impacting the beam pipe, in FLUKA terms referred to as a primary. This is important since different simulations may have a different number of primary particles, due to some runs requiring a lot of lost particles to obtain sufficient statistics. Further, detector region 1a is normally used for comparison of the secondary particle shower, since it is close enough to the beam line to get many particles entering it, and thus gives good statistics, while at the same time being at a location where a BLM detector may be installed.

6.1 Effect of the lost electron energy on the secondary particle shower

To see the effect of the beam energy on the secondary particle shower, simulations were done with three different initial electron energies of 85 MeV, 120 MeV and 150 MeV, corresponding to the minimum and maximum beam energy at the TBL. Using track-length estimators, the fluence of energy, electrons, positions, photons, neutrons and charged hadrons were calculated in the detector region shown in figure 5.4.

For all loss energies, the particle spectrum is dominated by electrons, positrons, gammas and neutrons. Protons, alpha particles and other light nucleons make an insignificant contribution to the spectrum and can be neglected in terms of energy deposition or the signal generated in a BLM. The fluence of shower particles at detector location 1a can

be found in figure 6.1. Within the energy range simulated, the initial energy of the lost electrons does not seem to have a significant effect on the secondary particle shower distribution. The effect of the lost electron energy on the secondary electron fluence in detector region 1a can be seen in figure 6.2.

6.2 Particle composition of secondary particle showers

In addition to measuring the fluences at the detector regions, a simulation was run where all secondary particles exiting the quadrupole were saved, using the first step of the two-step routines. It was calculated that more than 80 % of the total energy of the lost particles is absorbed in the beam pipe and magnet yoke and coils. Hence, it does not reach the region outside of the quadrupole, where detectors can be placed. The relative energy distribution and relative number of the secondary particles exiting the quadrupole is given in table 6.1.

Shower constituent	Relative energy	Relative count
Photons	51%	64%
Electrons	46%	28%
Positrons	2.7%	3.1%
Neutrons	0.3%	4.9%

Table 6.1: Relative distribution of energy and particle count for secondary particles exiting the quadrupole region after losses of 150 MeV electrons.

Electrons and photons make up most of the energy and the number of particles in the secondary particle shower. A BLM detector should therefore be sensitive to one or both of these particles.

6.3 Effect of the loss location on the secondary particle shower

To investigate the effect of the impact position of the beam, several simulations were performed where the impact location was varied. Four simulations were done where a narrow beam hits the beam pipe on the top, bottom, left and right side, at the longitudinal center of a defocusing magnet. In order to see the effect of the magnetic field, two more simulations were run with particles starting evenly distributed around the beam pipe, at a focusing and a defocusing quadrupole, and this is reported in section 6.5.

The resulting secondary particle showers from the four simulations where the beam impact the beam pipe at four different locations are very similar. The results from when the beam impacts the beam pipe towards the right looking upstream, i.e towards detector region 1a, is presented. The result for evenly distributed particles at a focusing and a

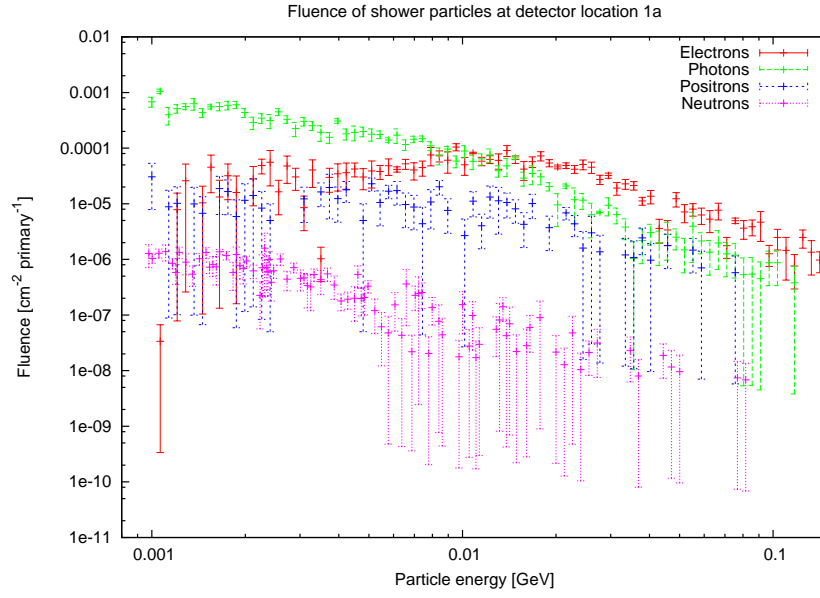


Figure 6.1: Fluence of various secondary particles at detector region 1a for losses of 150 MeV electrons.

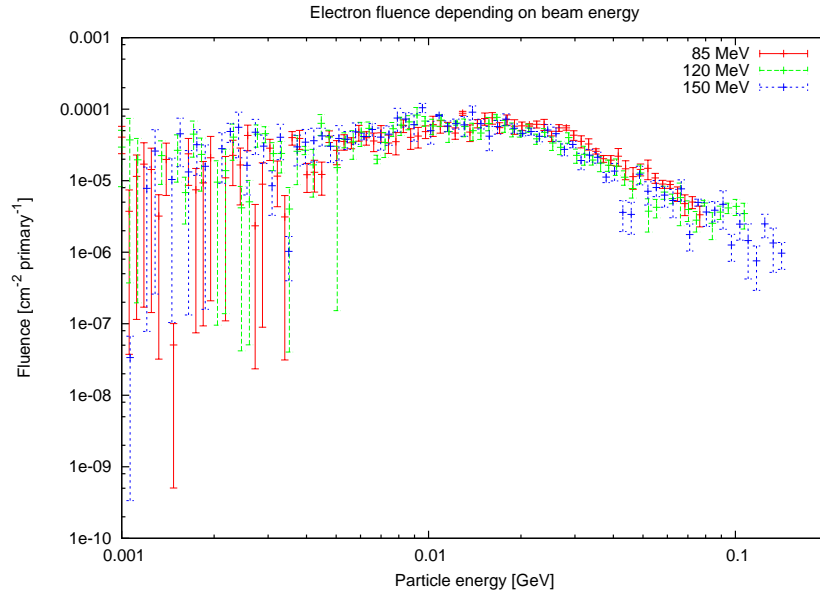


Figure 6.2: Fluence of secondary electrons at detector region 1a for various initial beam energies.

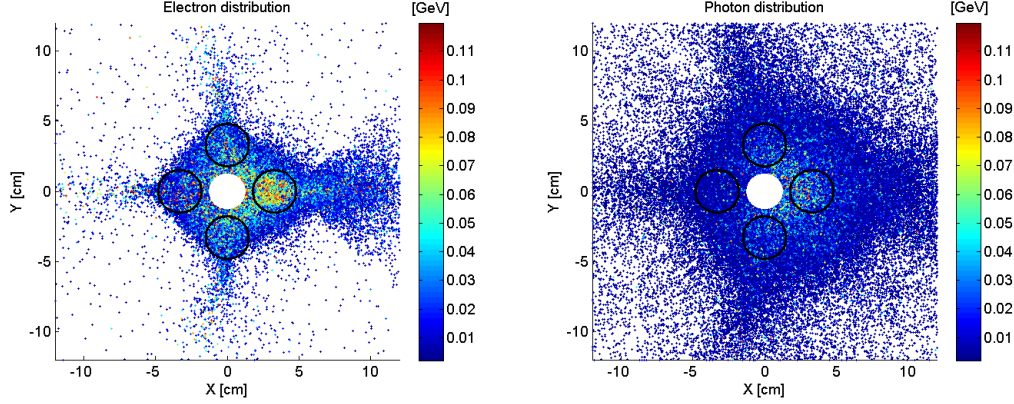


Figure 6.3: Particle shower after a quadrupole, with 0.15 GeV electrons lost inside the magnet. The loss occur at a single location in the beam pipe, to the right in the picture, at the direction of detector region 1a. Detector regions 5-8 are circled.

defocusing quadrupole are also very similar, and the result from the focusing quadrupole is presented. Figures 6.3 and 6.4 show the spatial distribution of electrons and photons passing through a plane perpendicular to the beam direction. The plane is located immediately downstream after the quadrupole at which the losses occur, at the same distance from the quadrupole as the detector regions. In the simulations, when a particle reaches this plane it is saved to file and not simulated further, and thus the plots are of the particles exiting a quadrupole, and does not include any backscattered particles.

In figures 6.3 (a) and 6.4 (a), the effect of the magnetic fields and absorption in the yoke and coil is clearly visible, with fewer electrons in the diagonal regions of the plot. Electrons with high energy can be found where there is a free path to the loss location, corresponding to detector regions 5-8. The distribution for positrons is very similar to that of the electrons, while the distribution for photons and neutrons is more uniform in the radial direction. The photon distribution is seen in figures 6.3 (b) and 6.4 (b).

6.4 Secondary particle fluence at different detector locations

The sensitivity of a detector to the initial loss depends strongly on its location, since the intensity of the secondary particle shower varies between different locations. The fluence of particles at the detector regions was simulated for when the beam is lost at the beam pipe towards detector region 1a. The result is similar for all particle types, and the fluence

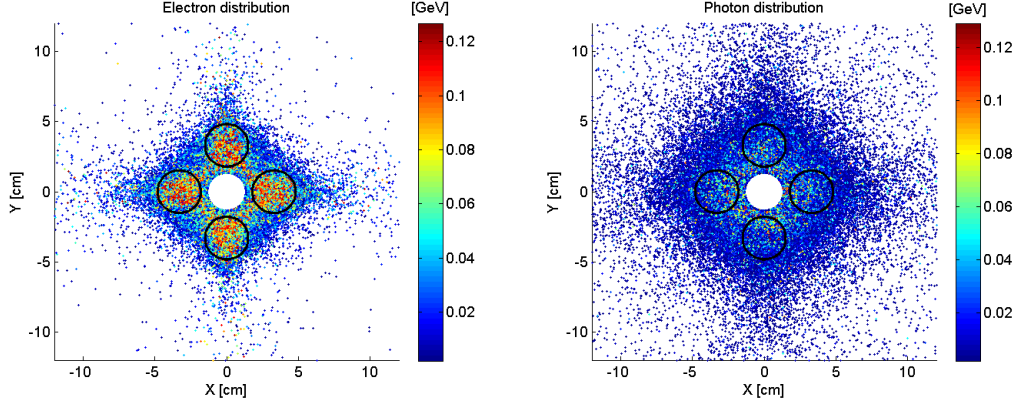


Figure 6.4: Particle shower after a quadrupole, with 0.15 GeV electrons lost inside the magnet. The losses are distributed evenly around the beam pipe. Detector regions 5-8 where particle fluences are recorded are indicated with circles.

of electrons will be presented. Figure 6.5 shows the fluence at regions 1 to 8, and figure 6.6 shows the electron fluence at detector region 1a to 1d, where detectors can be installed at the TBL.

As seen in section 6.3, the high-energy particles pass through detector regions 5-8. With the loss occurring closest to detector region 5, a significant increase of high-energy particles is seen at this region. Regions 6 and 8 show a very similar fluence, and region 7 has the lowest fluence of the detectors closest to the beam line. For regions 1-4, further from the beam line, region 1a has the highest fluence, while the other three regions show a similar fluence. The total fluence is shown in table 6.2. From this table, we can see that moving the detector from 3 to 10 cm from the beam line will decrease the fluence of particles, and thus the sensitivity, by about a factor of 20 to 30. Further, if the loss occur at a specific location, the nearest detectors will experience a fluence that is 5 to 10 times greater than the other detector regions at the same distance from the beam line.

At detector regions 1a to 1d a similar reduction of fluence can be found. The sensitivity of a detector at the TBL can thus be changed by a factor of 30 by adjusting the detector height. This must be taken into consideration when analysing detector signals, and when comparing simulated detector responses with measured ones.

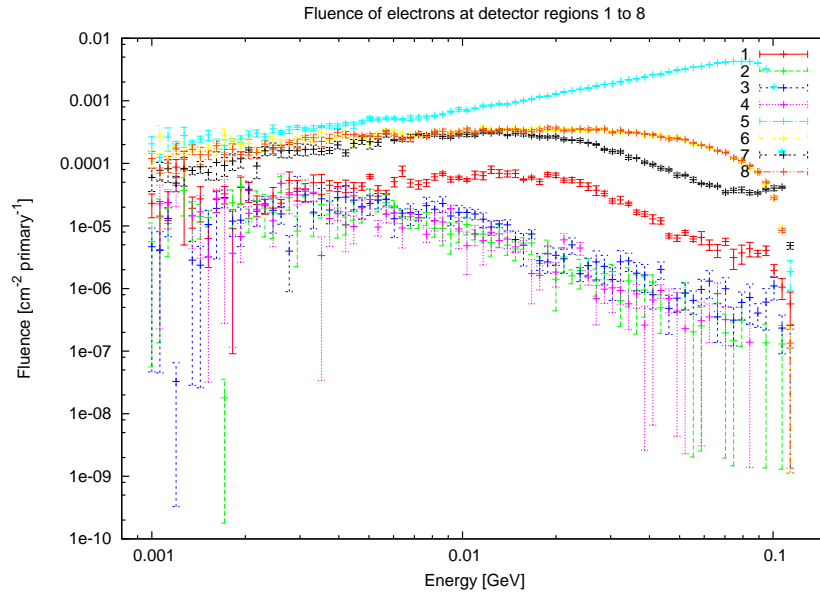


Figure 6.5: Fluence of electrons at detector regions 1-8 after a localized loss of 120 MeV electrons.

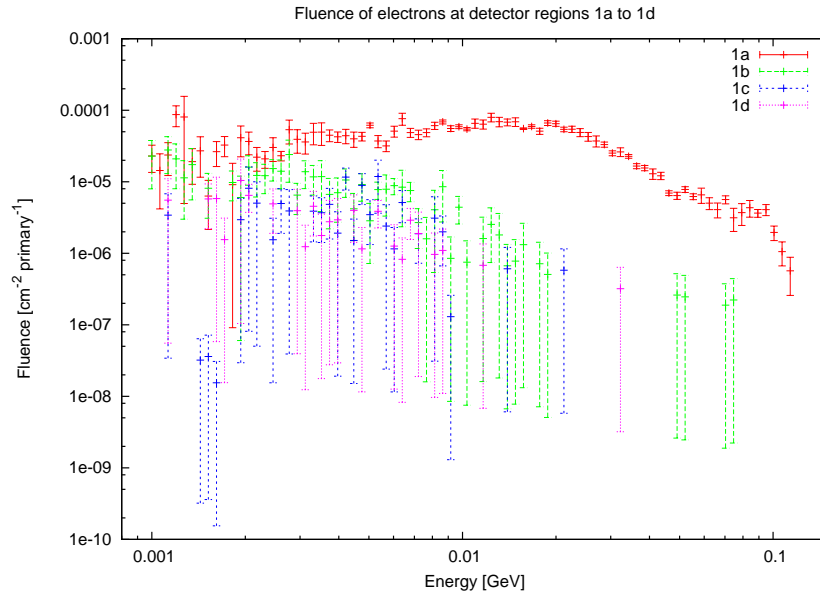


Figure 6.6: Fluence of electrons at detector regions 1a to 1d, corresponding to possible locations where detectors can be installed. The lost electrons had an energy of 120 MeV and were lost at a single location.

Detector region	Electron fluence [cm ⁻² primary ⁻¹]	Electron fluence relative to detector 1a
1a	$1.71 \cdot 10^{-4} \pm 3.4, \%$	1
1b	$2.25 \cdot 10^{-5} \pm 10.2, \%$	0.132
1c	$5.91 \cdot 10^{-6} \pm 11.0, \%$	0.035
1d	$4.59 \cdot 10^{-6} \pm 16.0, \%$	0.027
2	$4.69 \cdot 10^{-5} \pm 10.2, \%$	0.274
3	$4.98 \cdot 10^{-5} \pm 9.2, \%$	0.291
4	$4.56 \cdot 10^{-5} \pm 10.2, \%$	0.267
5	$6.11 \cdot 10^{-3} \pm 0.3, \%$	35.7
6	$1.17 \cdot 10^{-3} \pm 1.0, \%$	6.84
7	$7.78 \cdot 10^{-4} \pm 1.0, \%$	4.55
8	$1.14 \cdot 10^{-3} \pm 0.7, \%$	6.67

Table 6.2: Electron fluence at all detector regions, for a localized loss of 120 MeV electrons.

6.5 Effects of quadrupole type

A magnetic quadrupole focuses the beam in one plane and defocuses it in the other. Typically a quadrupole is referred to as a focusing magnet when it focuses in the horizontal plane. The effect of the quadrupole type on the secondary particle shower for a loss distributed evenly around the beampipe is not clearly visible in figure 6.4. To investigate this, the number and energy of the secondary particles entering the detector regions 5-8 were calculated. The location of detector regions 5-8 are indicated by the circles in figure 6.4 Table 6.3 shows the ratio of particles, and total energy in the horizontal detection regions to the vertical detection regions for a loss at a defocussing quadrupole.

Particle type	Total energy ratio Horizontal / Vertical	Particle count ratio Horizontal / Vertical
Photons	1.04	1.04
Electrons	1.11	1.10
Positrons	0.86	0.91
Neutrons	0.99	1.02

Table 6.3: Ratios of energy distribution and particle count for all vertical and horizontal detection regions for a beam loss at a focusing quadrupole.

For the charged particles, a noticeable difference between the horizontal and vertical regions can be found. For electrons about 10 % more particles are found in the horizontal regions. Positrons, which are oppositely charged to electrons, are defocused by the same magnetic field. The difference in total energy of the particles and total number of particles between horizontal and vertical regions is about the same as for electrons, but with more positrons in the horizontal regions. The photons are not electrically charged and thus

unaffected by the magnetic fields. However, as they are produced mainly through electron interactions, the photons are expected to roughly follow the electron distribution. An increase of 4 % is found for both photon energy and count in the horizontal regions. The neutron distribution is not significantly affected by the orientation of the magnetic field.

6.6 Effects of beam impact angle

To investigate the sensitivity of the shower distribution on the impact angle of the beam, four simulations were performed with impact angles of 0° , 1° , 5° and 10° relative to the beam pipe axis. The loss was represented at a single location and occurred in the horizontal plane. The particle fluence spectra for electrons, positrons, gammas and neutrons are estimated at a boundary just downstream of the quadrupole. The energy distribution for electrons and photons, being the main constituent of the showers, are shown in figures 6.7 and 6.8 respectively.

The spatial distribution of the energy deposition by the secondary particle shower is shown in figure 6.9. The energy deposition is averaged over a depth of 60 cm.

It is clear from the plots that the distribution of shower energies is similar for all loss angles. As the impact angle increases, the fluence of particles in the detector increases for all energies. For the 0° and the 10° case, the difference in total electron fluence is roughly a factor of 2, which can be seen in table 6.4.

If a particle is at the center of the beam pipe at one quadrupole and impacts the beam pipe at the center of the next one, it will do so at an angle of 0.5° . For normal operational losses, the impact angle is thus expected to be very small. The exact angular distribution of the lost particles for various modes of operation is not known. In the following sections a loss angle of 1° is used and it is not expected that estimates would vary significantly with loss angle for standard operational modes.

Impact angle	Electron fluence [cm ⁻² primary ⁻¹]	Electron fluence relative to 1° impact angle
0°	$1.35 * 10^{-4} \pm 4.7, \%$	0.73
1°	$1.85 * 10^{-4} \pm 9.8, \%$	1
5°	$2.20 * 10^{-4} \pm 2.8, \%$	1.19
10°	$2.60 * 10^{-4} \pm 3.9, \%$	1.41

Table 6.4: Electron fluence at detector region 1a for various impact angles of the initial loss.

6.7 Loss distribution along beamline

The position of the loss and the surrounding geometry can significantly affect the distribution of the resulting particle shower. In these simulations, the loss occur at the center of a quadrupole and much of the energy is absorbed in the quadrupole coils and yoke.

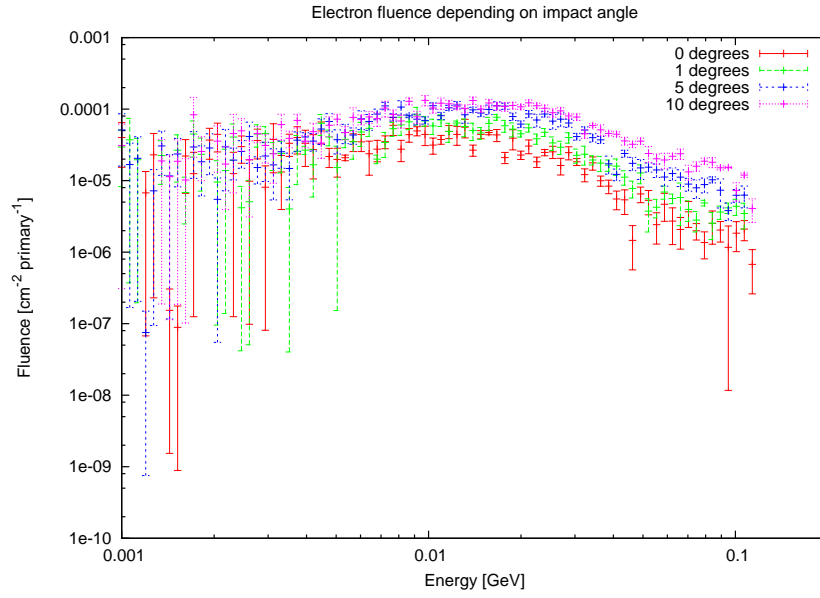


Figure 6.7: Electron fluence at detector location 1a for different impact angles.

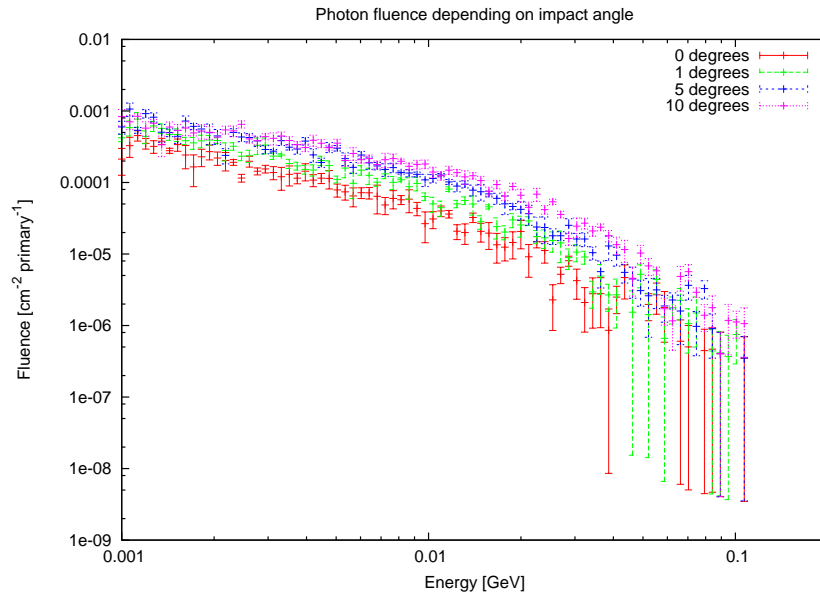
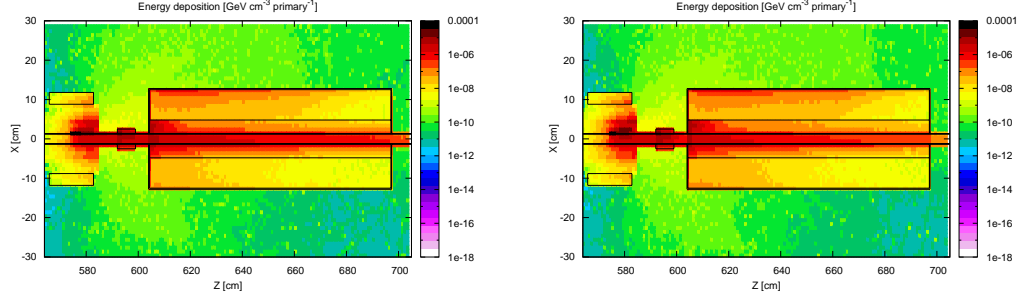
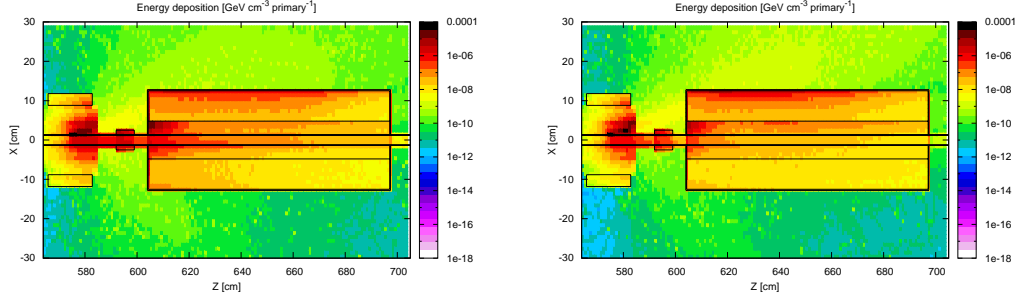


Figure 6.8: Photon fluence at detector location 1a for different impact angles.



(a) Energy deposition in the TBL for 0° impact angle. (b) Energy deposition in the TBL for 1° impact angle.



(c) Energy deposition in the TBL for 5° impact angle. (d) Energy deposition in the TBL for 10° impact angle.

Figure 6.9: Effect of the beam impact angle on the energy deposition in the TBL. The beam impacts at the center of the quadrupole at $X=1.2$ cm, at angles 0° , 1° , 5° and 10° . The energy deposition is averaged over a depth of 60 cm.

The secondary particles can be absorbed or scattered on surrounding elements such as the PETS, the support girder or the concrete walls before reaching the BLM. Since the loss showers are mainly forward directed, a BLM detector can also detect particles from losses occurring further upstream, and not only from losses at the nearest quadrupole.

Figure 6.10(a) shows the energy deposition in the TBL region resulting from losses at the fifth quadrupole. Although the losses start at a single location along the TBL, the resulting secondary particle showers reach all the regions surrounding the TBL. Nevertheless, as shown in figure 6.10(b), the fluence of secondary electrons at a consecutive downstream quadrupole is calculated to be over 2 orders of magnitude lower. This indicates that the BLM signal would be proportional to localised losses rather than being sensitive to ‘build up’ effects from upstream losses.

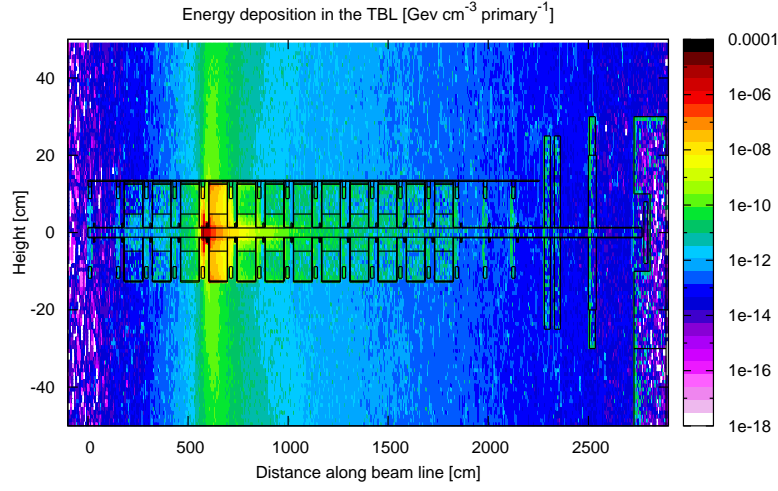
6.8 Loss scenario

Depending on the quadrupole type, the losses are not expected to occur in a single location as in the previous simulations, but rather in either the horizontal or vertical plane. A more accurate representation of the losses will be required for estimating the fluence and dose at detector locations, to be able to predict the signal from the detectors. Simulations were run with losses in the horizontal plane, the vertical plane, and for losses evenly distributed along the beam pipe. The electron fluence at detector locations 1a to 1d is shown in table 6.5. The beam impact angle is 1° for all considered losses.

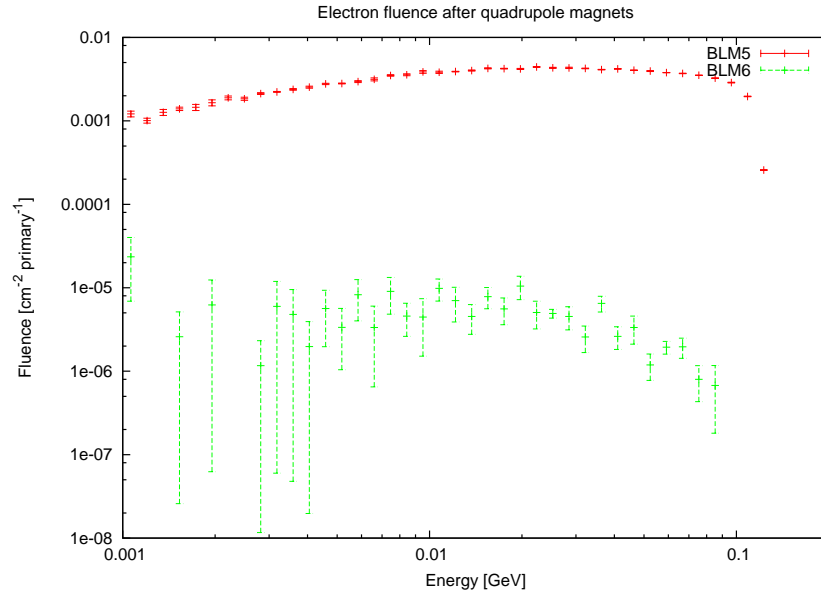
Loss scenario	1a	1b	1c	1d
Single impact location	1	1	1	1
Horizontal losses	0.7	0.7	1.1	0.5
Vertical losses	0.3	1.5	1.3	1.2
Evenly distributed losses	0.5	0.9	1.3	0.8

Table 6.5: Electron fluence at detector regions 1a to 1d for various loss scenarios compared to a loss at a single location.

Region 1a, being closest to the loss, sees the biggest difference in fluence. For the other regions, the difference is smaller, but still noticeable. For vertical losses the fluence is increased, while for horizontal and evenly distributed losses both increases and decreases are found. For all detector regions, the difference is small enough that the beam impacting a single location is a decent approximation to the actual loss.



(a) Energy deposition in the TBL due to losses at a single quadrupole.



(b) Electron fluence at detector locations. The loss occurs at the fifth quadrupole, and the electron fluence is estimated at detectors locations by the fifth and sixth quadrupole.

Figure 6.10: Effect of losses at one quadrupole at subsequent BLM location. Losses occur at the fifth quadrupole, and the fluence of electrons is measured in detector regions immediately downstream of the fifth and sixth quadrupole.

Chapter 7

Other simulated loss scenarios

Losses at quadrupoles are the most likely loss scenarios, although losses at other locations can also result in a measurable secondary particle fluence at the detector locations. This is especially important for the Cherenkov fiber, since it will measure the shower along the entire TBL. Several simulations were run to estimate the effects of losses occurring at other locations than the quadrupoles, such as the BPMs, the PETS and the beam dump.

7.1 Uniform losses along the TBL

To estimate the signal from the localised BLMs and the Cherenkov fiber installed at the TBL, losses at every quadrupole must be considered. A FLUKA source routine has been developed to distribute the lost electrons along the TBL. The routine allows for the starting particles to be distributed evenly between the 16 quadrupoles, or to use a user-specified probability distribution to define the probability that a particle starts at each quadrupole. The particles can either be distributed evenly on the beam pipe, or only occur in a given plane that alternates between the quadrupoles, following the FODO lattice. The impact angle between the particles and the beam pipe can also be specified. The time structure of the losses is relevant, particularly in the case of the Cherenkov fiber signal. Whilst the length of the pulse, or bunch train, entering the TBL can vary depending on the combination scheme, in this simulation it was assumed to be 240 ns. To see the effect of the beam train passing through the TBL on the Cherenkov fiber signal, each particle is given a random position in the time structure of the train. The particle is given a starting time depending on which quadrupole it starts from and where in the train it is situated. An example of simulated absorbed dose in the TBL due to uniform losses is shown in figure 7.1.

7.2 Losses at BPM and PETS

While the losses at the TBL are expected at the quadrupoles since the beam size is largest there, simulations were also done with losses at other locations. Three different scenarios were simulated, with losses at a BPM, at the beginning of a PETS and at the end of

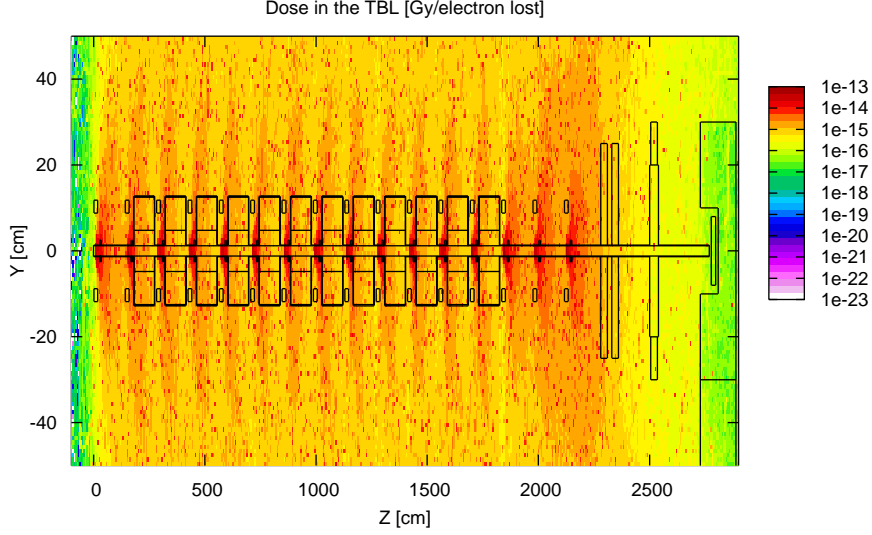


Figure 7.1: Absorbed dose in the TBL resulting from losses at every quadrupole. Values are averaged over a width of 1 m.

a PETS. Since the detector regions are immediately after a quadrupole, the fluence was measured both for the closest upstream and downstream detector regions for each loss. The losses were simulated starting at a single location, impacting the beam to the same direction as detector region 1a. The electron fluence is shown in figure 7.2 for the upstream detector and in figure 7.3 for the downstream detector.

For the upstream detectors, only losses at a BPM result in a noticeable fluence of electrons. This fluence is however at least one order of magnitude less than the one resulting from losses at quadrupoles. For losses at a PETS, the secondary particle shower is negligible at the detector locations. For the downstream detectors, losses at a BPM and at the beginning of a PETS give similar fluences that are more than one order of magnitude lower than the one resulting from losses at a quadrupole. Losses at the end of a PETS are the only ones that give a significant fluence at the detector. This fluence is a factor 3 lower than the one from a quadrupole loss. Thus, the losses that contributes to a detector signal are primarily losses at quadrupoles, but if there are significant losses just before a quadrupole these must be taken into account. The simulated fluences are shown in table 7.1.

7.3 Beam dump

After the beam has passed through the 16 TBL modules, it will pass through two final quadrupoles and a dipole before hitting the beam dump. There, the beam is stopped by

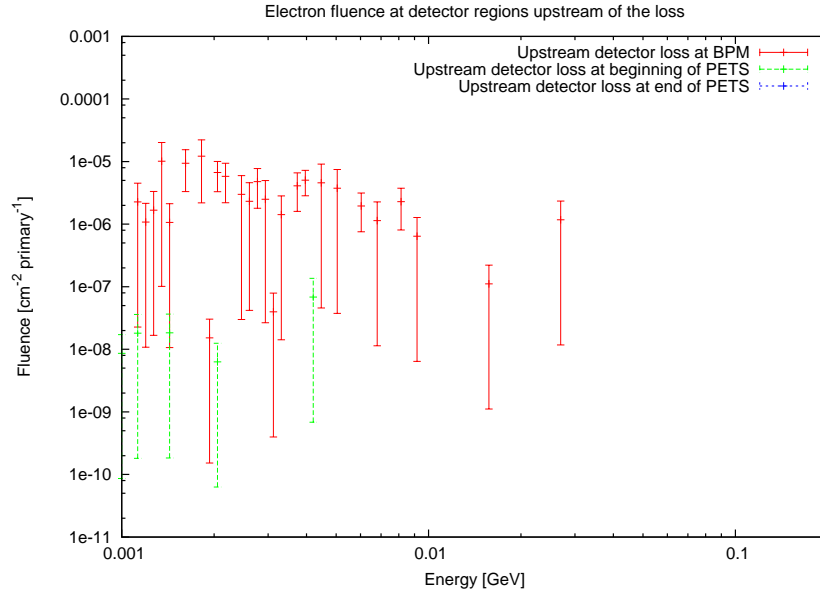


Figure 7.2: Electron fluence at detector region 1a for the nearest upstream detector location. Losses occur at three different locations.

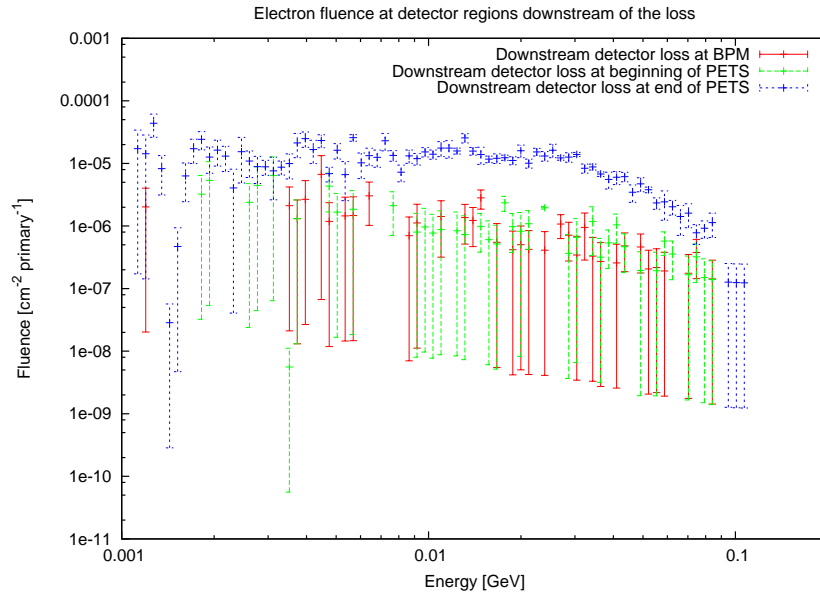


Figure 7.3: Electron fluence at detector region 1a for the nearest downstream detector location.

Loss scenario	Electron fluence [cm ⁻² primary ⁻¹]	Electron fluence relative to quadrupole loss
Quadrupole loss	$1.07 \cdot 10^{-4} \pm 3.4, \%$	1
Upstream detectors		
Loss at BPM	$5.34 \cdot 10^{-6} \pm 23, \%$	0.05
Loss at start of PETS	$7.18 \cdot 10^{-9} \pm 57, \%$	$6.7 \cdot 10^{-5}$
Loss at end of PETS	$0 \pm 0, \%$	—
Downstream detectors		
Loss at BPM	$2.34 \cdot 10^{-6} \pm 15, \%$	0.02
Loss at start of PETS	$3.24 \cdot 10^{-6} \pm 11, \%$	0.03
Loss at end of PETS	$5.11 \cdot 10^{-5} \pm 4.3, \%$	0.47

Table 7.1: Electron fluence at detector region 1a for various loss locations. The fluence is estimated at both the nearest upstream and downstream detector.

a block of graphite, and the surrounding concrete blocks most of the resulting radiation. Some radiation may however escape the dump and could be detected by the BLM system. A simulation was run with particles impacting the beam dump, to estimate the effects on the detectors. The energy deposition resulting from a beam dump can be seen in figure 7.4.

In the FLUKA model, the final quadrupole is located at 2120 cm downstream of the start of the TBL, and one ACEM is installed after this quadrupole. As seen in figure 7.4, only a few particles reach this region, and no fluence of particles was measured in the simulation for several detector locations. The final three magnets stop the particles from reaching the detector regions at the 16th quadrupole, and the fluence resulting from a beam dump is thus negligible for localized detectors.

In the simulations, a simplified magnet model was used for the final quadrupoles and dipole, where they are solid blocks of an iron-copper mixture at half density, to account for the air gaps. In reality, it might be possible for some secondary shower particles to pass through the air gaps and reach the detector location. Even so, the fluence at the detector location due to losses at the quadrupole is expected to be much greater than the fluence due to the beam dump, so the effect of the beam dump can be neglected for the localized detectors.

For a Cherenkov fiber installed 28 cm above the beam line, the signal generated at the TBL modules due to the beam dump is also negligible. The fiber carrying the signal out of the CLEX hall will have to extend beyond the TBL modules, and may have to pass through a region where the beam dump can generate a signal. This will result in additional background signal that must be accounted for. The fiber should be installed so that the secondary shower particles from the dump enters the fiber perpendicularly to the fiber axis. The Cherenkov photons produced will then not be in the acceptance cone, and will not propagate to the fiber end.

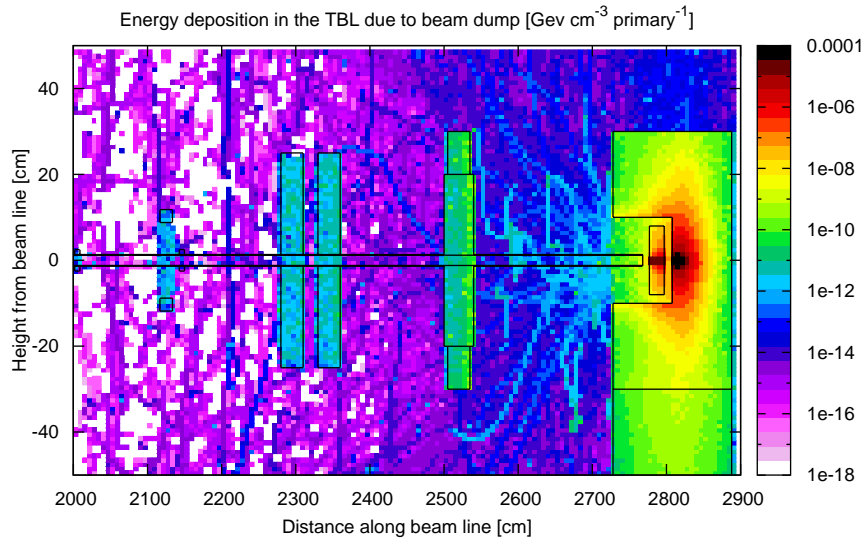


Figure 7.4: Spatial distribution of the energy deposition in the TBL due to the beam dump. Values are averaged over a width of 1 m

Chapter 8

Estimate of BLM signals from simulations

Based on the simulated characteristics of the secondary particle showers at the detector locations, the BLM response function can be estimated. All detectors installed at the TBL give a current pulse as output when subjected to radiation, and the detector response will be given with respect to both absorbed dose and electron fluence. Since all detectors are sensitive to electrons, but not necessary to photons or other particles, signal estimates based on dose should overestimate the sensitivity while estimates based on electron fluence should underestimate the sensitivity. This gives an upper and a lower limit to the sensitivity and thus the beam losses, as well as a double-check that the values obtained are sensible. The final goal is to combine the detector intrinsic sensitivity with the simulated secondary particle shower, to obtain a BLM response expressed in signal generated per electron lost in the TBL. In general, the installed detectors are almost exclusively sensitive to electrons and have little sensitivity to photons, so calculations based on electron fluences are expected to be the most accurate.

8.1 Detector settings and sensitivity

The sensitivity of a detector can be varied greatly by adjusting its supply voltage, position and the angle at which it faces the quadrupole. During the TBL run, the main focus has been on the combination scheme, and the total beam current has been increasing as the tests progressed. This also means that the beam losses have been increasing, and the detector settings have been adjusted several times since some detectors saturated as the beam losses increased, and their sensitivity had to be reduced. The detector sensitivity will be estimated for the settings used by the end of the TBL run, since by then all detectors had been installed and appropriate settings had been found.

A useful conversion factor is given in [4], for converting dose into MIP fluence. By expressing a dose as an energy deposition per mass, and assuming that a MIP deposits $2 \text{ MeV}/(\text{g}/\text{cm}^2) = 3.2 \cdot 10^{-10} \text{ J}/(\text{kg}/\text{cm}^2)$, it is possible to express dose as a fluence of MIP/cm^2

$$1\text{Gy} = 1 \frac{\text{J}}{\text{kg}} \cdot \frac{\text{MIP} \cdot \text{kg}}{3.2 \cdot 10^{-10} \cdot \text{J cm}^2} = 3.1 \cdot 10^9 \frac{\text{MIP}}{\text{cm}^2}$$

Given a detector with a known size, this relation allows for converting between sensitivity expressed in dose to one expressed in MIP fluence.

8.1.1 ACEM

The ACEMs installed were manufactured by Hamamatsu, and the detector type, radiation monitor R3807, is no longer being manufactured. Although ACEMs have been used at CERN before, they have mostly been used to detect relative beam losses, and not to estimate the magnitude of the loss. For this reason, information about the ACEM sensitivity is somewhat limited. Useful data about the ACEM performance can be found in [4].

Assuming that 5% of the incident radiation produces secondary electrons that are detected, that the ACEM gain is 10^4 , and using that the detector area is 11.3 cm^2 , a total sensitivity of

$$3.1 \cdot 10^9 \frac{\text{MIP}}{\text{cm}^2 \text{ Gy}} \cdot 11.3 \text{ cm}^2 \cdot 0.05 \frac{\text{e}}{\text{MIP}} \cdot 1.6 \cdot 10^{-19} \frac{\text{C}}{\text{e}} \cdot 10^4 = 2.8 \cdot 10^{-6} \frac{\text{C}}{\text{Gy}}$$

is obtained. If the conversion from MIP fluence to dose is ignored, the sensitivity is instead $9.0 \cdot 10^{-16} \text{ C/MIP}$.

8.1.2 PEP-II

For the sensitivity of the PEP-II detector, three factors are important: How many Cherenkov photons are generated by a particle crossing, how efficiently they are collected and converted into photoelectrons, and the Photomultiplier tube (PMT) gain. In [4] suggested values are $dN/dx = 227 \text{ photons}/(\text{MIP cm})$ in fused silica, 80% of the generated Cherenkov photons reach the PMT, and the PMT detects 30% of all photons. The installed detector has a radiator with a volume of 1 cm^3 . The total Cherenkov photon production then becomes

$$3.1 \cdot 10^9 \frac{\text{MIP}}{\text{cm}^2 \text{ Gy}} \cdot \frac{227 \text{ photons}}{\text{MIP} \cdot \text{cm}} \cdot 1 \text{ cm}^3 = 7 \cdot 10^{14} \frac{\text{photons}}{\text{Gy}}$$

The photomultiplier used in the PEP-II detector is a Hamamatsu R5600-U3, and it was supplied with -510 V giving a PMT gain of 10^4 . With the stated collection and detection efficiencies, the sensitivity becomes

$$7 \cdot 10^{14} \frac{\text{photons}}{\text{Gy}} \cdot 0.8 \cdot 0.3 \cdot 1.6 \cdot 10^{-19} \frac{\text{C}}{\text{e}} \cdot 10^4 = 2.7 \cdot 10^{-4} \frac{\text{C}}{\text{Gy}}$$

The fused silica radiator is a cylinder with a height of 1 cm and a diameter of 1.1 cm. Assuming that a particle traverses 1 cm of the radiator on average, and using the efficiency and gain as above, the sensitivity is

$$223 \frac{\text{photons}}{\text{MIP}} \cdot 0.8 \cdot 0.3 \cdot 1.6 \cdot 10^{-19} \frac{\text{C}}{\text{e}} \cdot 10^4 = 8.7 \cdot 10^{-14} \frac{\text{C}}{\text{MIP}}$$

8.1.3 Diamond

The detector is a pCVD diamond detector manufactured by cividec, used without any amplification or filtering. A MIP will deposit $1.725 \text{ MeV}/(\text{g}/\text{cm}^2)$ [5], and multiplied with the diamond density of $3.52 \text{ g}/\text{cm}^3$, this gives an energy deposition of $6.07 \text{ MeV}/\text{cm}$. The detector is $8 \cdot 8 \text{ mm}$ in size, with a thickness of $500 \mu\text{m}$. A MIP passing through a diamond of this thickness will thus deposit 0.3 MeV . The average energy needed to create an electron-hole pair in diamond is 13 eV , so one MIP crossing creates $2.32 \cdot 10^4$ pairs. The diamond has been supplied with a bias voltage of $+300 \text{ V}$, or $0.6 \text{ V}/\mu\text{m}$ which gives a collection efficiency of 0.3 [32], so that 30% of the electron-hole pairs contribute to a signal. The total charge generated by a MIP passing through that can be measured is thus

$$2.32 \cdot 10^4 \cdot 2 \cdot 0.3 \cdot 1.5 \cdot 10^{-19} = 2.23 \cdot 10^{-15} \text{ C/MIP}$$

since an electron-hole pair has twice the elementary charge. The values used here are based on pure diamond without defects, so for a pCVD diamond the total charge is about $1/3$ of a defect-free diamond [26]. The total sensitivity thus becomes $0.75 \cdot 10^{-15} \text{ C/MIP}$.

For sensitivity with respect to dose, we note that the diamond has a mass of 0.11 g based in its size and density. One electron-hole pair, or two charges, is generated by 13 eV , so that with a collection efficiency of 30% we get

$$\frac{2\text{e}}{13\text{eV}} \cdot 0.3 = 4.6 \cdot 10^{-2} \frac{1}{\text{kg}} \cdot \frac{\text{C}}{\text{Gy}}$$

Multiplied by the detector mass, and adjusting for that a pCVD diamond will have one third the signal, the sensitivity becomes $1.7 \mu\text{C}/\text{Gy}$.

8.1.4 Cherenkov fiber

The sensitivity of the fiber is mainly affected by the fibers that carry the signal out of the experimental hall and to the detectors, and by the detector itself. The fibers are connected by an optical coupler, and these have been measured to let 80% of the signal through to the next fiber. Next, the fiber that carries the upstream signal to the detector is 75 m long, and the downstream one is 50 m . For optical photons, the attenuation is on average $20 \text{ dB}/\text{km}$, which results in transmission efficiencies of 71% and 79% respectively.

The MPPC that converts the photons to a current is situated at a distance from the fiber end, to allow the photons to spread out and hit the entire MPPC surface. For the upstream signal, this distance has remained constant, while different distances have been tried for the downstream signal. When treated as a ray, there are two kinds of photons that can propagate in a multimode fiber. Meridional rays always pass through the fiber axis after every reflection, and skew rays do not pass through the centre, instead propagating in a helical fashion. When entering or exiting the fiber, there is a maximum angle with respect to the fiber axis that will allow the photon to propagate inside the fiber. If the

angle is higher, total internal reflection will not occur, and the photon will not propagate. Only photons within the ‘cone of acceptance’ will be propagated. The size of the cone is different for the two types of rays, and is larger for skew rays.

The distance between the MPPC and the fiber has been 1 cm at the upstream detector, which makes the MPPC cover a maximum amount of the cone of acceptance for the meridional photons, but no part of the MPPC is outside the cone. This means that 63 % of all meridional photons are detected, while the highly skewed photons will not be detected. These skewed photons would because of their longer path length in the fiber arrive later than the meridional rays, and contribute to a smearing out of the signal. This causes problems when trying to reconstruct the loss from the signal, and the choice was made to sacrifice sensitivity for resolution. Assuming that the photons exit the fiber evenly spread out, an efficiency of 63 % is found for the upstream end. For the data taken at CTF-3 that is of interest, the downstream distance was 2 cm, so an efficiency of 16 % can be assumed.

The MPPC is a Hamamamtsu S10362-025C, and for photons with a wavelength in the range 350 to 600 nm, an average photon detection efficiency of 40 % is found in the data sheet. The MPPC has been supplied with 71.6 V, and then has an amplification of $3.4 \cdot 10^5$. This gives a total sensitivity of the detector of $7.8 \cdot 10^{-15}$ C/photon for the upstream detector, and $2.2 \cdot 10^{-15}$ C/photon for the downstream one.

There is one final conversion that occurs before the signal can be measured. A current-to-voltage converter with $U/I = 500$ turns the signal into a voltage. This voltage passes through a 50Ω resistor before exiting the box. The measuring device is expected to be terminated with another 50Ω resistance, so due to voltage division half the signal is measured. In total, the voltage must be divided by a factor of $500/2 = 250$ to convert the measured voltage into the MPPC generated current.

8.1.5 Estimated error

In calculating the detector sensitivities, several assumptions were made, that can contribute to an error in the calculation. Since the assumptions may only be considered as a good approximation, the error should be estimated. Sources of uncertainties can be:

- Voltage drift.

The supply voltage may not be entirely stable, and will then drift over time. For the diamond, this affects the charge collection negligibly, but for photomultiplier tubes, a change of one or two volts could change the gain by 2 to 3 %. The MPPC gain would also change with the high voltage. During the tests, the MPPC voltage was not observed to change more than 0.1 V, which corresponds to a change in gain of 3 %.

- Treating all electrons as MIPs.

In calculations based on electron fluence, it has been assumed that each electron is a MIP, which is only applicable for electrons with an energy above 1 MeV. In the simulations, the electrons have had an energy mainly between 1 and 150 MeV, with few electrons having an energy below 1 MeV. Further, the MIP energy deposition used

has been near the maximum of what a MIP can deposit in a material, which compensates that some electrons have higher energy and thus greater energy deposition. In total, an error of 10 % for using MIPs can be assumed.

- Detector angle.

When particles hit the detector, they do so at an angle to the detector surface normal, and this angle has been 0° in the sensitivity calculations. In the simulations it was found that more than 70 % of all particles impacts with an angle less than 30° . A particle impacting at this angle will travel 15 % longer inside the detector sensitive area, so a 10 % error can be assumed from not taking into account the angular sensitivity of the detector. Data about the angular sensitivity for the detectors are however unavailable, which prevents a more accurate calculation.

- Sensitivity assumptions.

Information about detection efficiencies are believed to be accurate, but depending on the specific detectors other efficiencies may be obtained. A 10 % error is estimated from these assumptions.

- Loss scenario.

In previous simulations, an up to 30 % change in electron fluence and dose was found for different loss scenarios compared to the simulated loss at a single location, such as horizontal, vertical, or evenly distributed losses. Since the exact nature of the losses are unknown, an additional error of this size must be considered.

8.1.6 Detector sensitivity summary

A summary of all the detector sensitivities is presented in tables 8.1 and 8.2. For the ACEM, PEP-II and diamond, the sensitivity is given in C/Gy or C/MIP, since these quantities are easily estimated by FLUKA. For the Cherenkov fiber, a matlab script has been developed [33] to give the number of photons exiting the fiber as a function of the particle energy and impact angle of particles entering the fiber. The sensitivity is given as signal generated per Cherenkov photon produced in the fiber.

Detector type	Sensitivity [C/Gy]		Sensitivity [C/MIP]	
	Range	Median	Range	Median
ACEM	$1.5 \cdot 10^{-6} - 4.5 \cdot 10^{-6}$	$2.8 \cdot 10^{-6}$	$4.5 \cdot 10^{-16} - 1.6 \cdot 10^{-15}$	$9.0 \cdot 10^{-16}$
PEP-II	$1.5 \cdot 10^{-4} - 4.4 \cdot 10^{-4}$	$2.7 \cdot 10^{-4}$	$4.3 \cdot 10^{-14} - 1.6 \cdot 10^{-13}$	$8.7 \cdot 10^{-14}$
Diamond	$9.5 \cdot 10^{-7} - 2.8 \cdot 10^{-6}$	$1.7 \cdot 10^{-6}$	$3.7 \cdot 10^{-16} - 1.3 \cdot 10^{-15}$	$7.5 \cdot 10^{-16}$

Table 8.1: Various detector sensitivities at the settings that they have been used at.

Fiber end	Sensitivity [C/photon]		Conversion factor U to I
	Range	Median	
Upstream	$4.3 \cdot 10^{-15} - 1.3 \cdot 10^{-14}$	$7.8 \cdot 10^{-15}$	1/250
Downstream	$1.2 \cdot 10^{-15} - 3.6 \cdot 10^{-15}$	$2.2 \cdot 10^{-15}$	1/250

Table 8.2: Cherenkov fiber sensitivities at the settings that they have been used at.

8.2 Simulated particles at detector locations

Additional simulations were run to estimate the deposited energy and the electron fluence at the detector locations. To estimate these values for the ACEM and for the diamond, the detector regions were set to aluminium or carbon at diamond density. The distance between the detector and the quadrupole was also changed, to correspond to where the sensitive part of the detector can be located. The height of the detector regions remained the same. The simulated values for dose and electron fluence for the ACEM and diamond are shown in tables 8.3 and 8.4.

ACEM		
Distance below beamline [cm]	Electron fluence [cm ⁻² primary ⁻¹]	Dose [Gy primary ⁻¹]
0	$4.2 \cdot 10^{-4} \pm 1.6\%$	$1.5 \cdot 10^{-13} \pm 6.2\%$
10	$9.7 \cdot 10^{-5} \pm 5.7\%$	$4.6 \cdot 10^{-14} \pm 21\%$
20	$3.3 \cdot 10^{-5} \pm 24\%$	$1.5 \cdot 10^{-14} \pm 24\%$
30	$2.0 \cdot 10^{-5} \pm 15\%$	$9.5 \cdot 10^{-15} \pm 47\%$

Table 8.3: Electron fluence and dose at ACEM detector locations.

Diamond		
Distance below beamline [cm]	Electron fluence [cm ⁻² primary ⁻¹]	Dose [Gy primary ⁻¹]
0	$1.4 \cdot 10^{-4} \pm 3.9\%$	$5.4 \cdot 10^{-14} \pm 16\%$
10	$6.2 \cdot 10^{-5} \pm 2.1\%$	$3.1 \cdot 10^{-14} \pm 29\%$
20	$2.8 \cdot 10^{-5} \pm 6.7\%$	$1.3 \cdot 10^{-14} \pm 21\%$
30	$1.7 \cdot 10^{-5} \pm 15\%$	$6.3 \cdot 10^{-15} \pm 34\%$

Table 8.4: Electron fluence and dose at diamond detector locations.

The PEP-II detectors were originally developed for use at the PEP-II accelerator, to be used in locations with intense synchrotron radiation that is part of normal operation. To shield the photomultiplier tubes from the synchrotron radiation, a 5 mm lead shielding surrounds it. To investigate the effect of the shield, simulations were run both with and without it, although only values with the shield are useful for estimating the BLM

signal. The simulated location of the detector matches the installed detector, and dose and electron fluence was simulated for the fused silica Cherenkov radiator in the PEP-II.

The effect of the lead shield is similar for electrons and photons, and the results for electrons are shown in figure 8.1. The lead shielding reduces the fluence of electrons reaching the fused silica region, with a greater reduction for the high-energy electrons, and thus reduces the sensitivity of the detector. As no synchrotron light is generated by the TBL, a lighter shielding that stops background photons in the visible light range could be used if necessary. The total electron fluence in the fused silica region is reduced by a factor of about 4 when the lead shield is present, and the same reduction is seen for the dose. For better statistics, the comparison simulations were done with the detector closer to the beam line. The electron fluence and dose at the actual detector location is shown in table 8.5. Due to the lead shielding and the detector location, too few particles enter the sensitive region to get good statistics. The simulated dose has varied over two orders of magnitude in the different simulations, which makes it difficult to estimate the error.

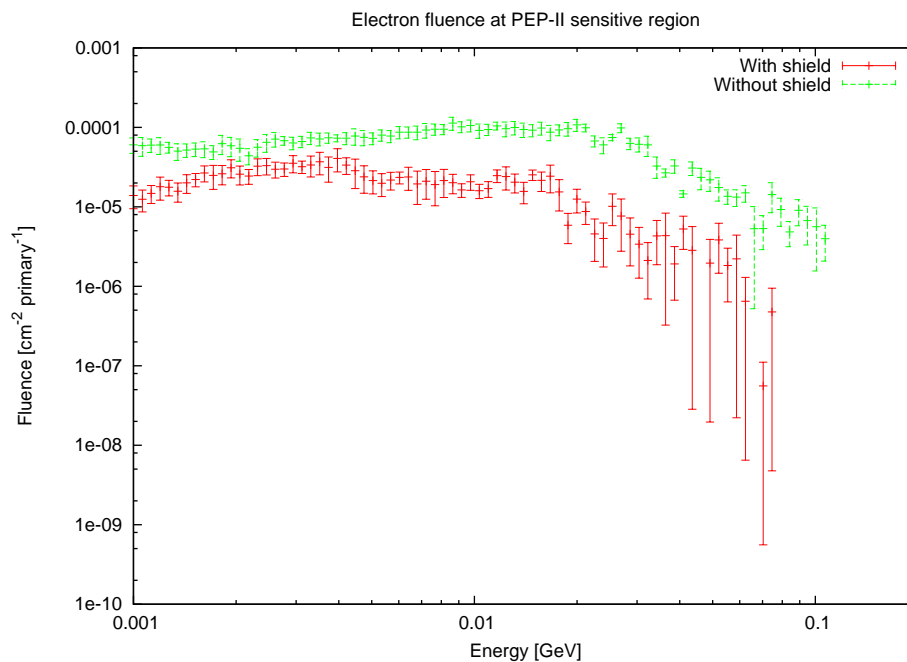


Figure 8.1: Electron fluence in PEP-II sensitive region, with and without the lead shielding.

PEP-II	
Electron fluence [$\text{cm}^{-2} \text{ primary}^{-1}$]	$4.8 \cdot 10^{-7} \pm 45\%$
Dose [Gy primary^{-1}]	$3.5 \cdot 10^{-16} \pm 95\%$

Table 8.5: Electron fluence and dose at PEP-II sensitive volume, with the lead shield included.

A previously developed matlab script [16] [33] predicts the signal generated in a Cherenkov fiber based on the particle type, position, momentum and time since loss of initial electron of all simulated particles entering the fiber region. Attenuation along the fiber is also taken into account. The resulting signal in terms of the time distribution of the generated photons at both the upstream and downstream end was calculated assuming uniform losses along the TBL, so that the same charge is lost at each quadrupole. The signal for a fiber installed 28 cm above the beamline, running parallel to it, is shown in figure 8.2.

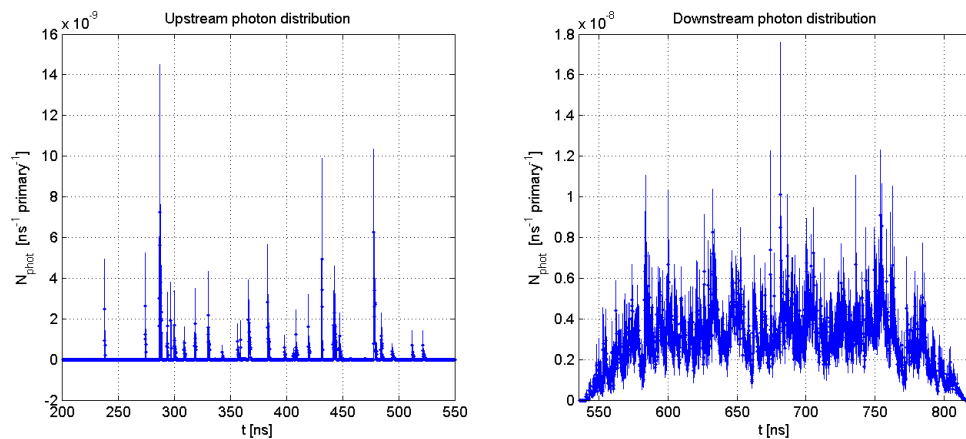


Figure 8.2: Simulated signal from a Cherenkov fiber installed 28 cm from the beam line.

For the downstream signal of the fiber, the time distribution for the arrival of photons is fairly uniform. Typically fiber BLM systems are used at facilities with short bunches, often less than 1 ns. With sufficiently fast photon detectors and electronics, the location of the loss can then be found from the time structure of the light pulse. However, due to the high bunch frequency at CTF3 one must consider the bunch train, assumed to be 240 ns in these calculations, which is similar to the length of the fiber. Therefore more sophisticated techniques must be used to determine the loss locations from the photon arrival times [33]. The simulations also save the particles entering the other two fiber regions implemented in the simulation. Using the matlab script to estimate the signal from these fibers shows that only a handful of photons can be expected to exit a fiber at these locations. A fiber at any of these locations is not expected to be sensitive enough to give the resolution needed for a longitudinal analysis. The number of photons exiting each fiber end is given by table 8.6 for a fiber installed close to the beam line.

	Photons at fiber end [photons/primary]
Upstream	$1.8 \cdot 10^{-7} \pm 94\%$
Downstream	$4.1 \cdot 10^{-6} \pm 30\%$

Table 8.6: Simulated estimate of photons exiting the Cherenkov fiber ends.

8.3 Estimated BLM signal

With the information about the expected dose and fluences in the detector, as well as the detector response at the voltages they have been used with, the detector sensitivity can be calculated. The diamond detector has its front face 20 cm below the beam line, so estimates for detector region 1c are applicable. The ACEM is installed 26 cm below the beam line, so an average of detector region 1c and 1d will give a good estimate. The PEP-II is installed 30 cm below the beam line, and the simulation puts it at the correct position. Likewise, the fiber is installed 28 cm above the beam line, at the same place as it has been simulated.

The active area of the ACEM is 11.3 cm^2 , for the diamond it is 0.64 cm^2 . The PEP-II has an active volume of 1 cm^3 , and under the assumption that a particle traverses 1 cm on average, the effective area becomes 1 cm^2 .

Multiplying together the values for sensitivity, for secondary particle shower estimates and for detector size, the BLM response is obtained for the installed detectors. The response for the localised detectors is given in table 8.7 and 8.8 for a sensitivity calculated from electron fluence and dose considerations respectively. The response of the Cherenkov fiber is given in table 8.9.

Detector	Response [C/lost electron]	
	Range	Median
ACEM	$9.3 \cdot 10^{-21} - 5.0 \cdot 10^{-20}$	$2.3 \cdot 10^{-20}$
PEP-II	$1.1 \cdot 10^{-20} - 1.1 \cdot 10^{-19}$	$4.2 \cdot 10^{-20}$
Diamond	$9.7 \cdot 10^{-21} - 4.0 \cdot 10^{-20}$	$2.1 \cdot 10^{-20}$

Table 8.7: Response of the localised detectors installed at the TBL based on electron fluence estimated.

Detector	Response [C/lost electron]	
	Range	Median
ACEM	$1.3 \cdot 10^{-20} - 7.6 \cdot 10^{-20}$	$3.5 \cdot 10^{-20}$
PEP-II	$2.6 \cdot 10^{-21} - 3.0 \cdot 10^{-19}$	$9.5 \cdot 10^{-20}$
Diamond	$9.8 \cdot 10^{-21} - 4.4 \cdot 10^{-20}$	$2.2 \cdot 10^{-20}$

Table 8.8: Response of the localised detectors installed at the TBL based on dose estimates.

Detector	Response [C/lost electron]	
	Range	Median
Upstream	$3.7 \cdot 10^{-23} - 4.4 \cdot 10^{-21}$	$1.4 \cdot 10^{-21}$
Downstream	$2.5 \cdot 10^{-21} - 1.9 \cdot 10^{-20}$	$9.0 \cdot 10^{-21}$

Table 8.9: Response of the Cherenkov fiber installed at the TBL.

Chapter 9

Measurements at CTF-3

With the information from the previous chapter about the response of each detector to a lost electron in the TBL, the amount of beam loss can be calculated from the measured BLM signals. At the beginning of the TBL test period, work was focused on installing the detectors and finding appropriate settings for voltage supplies. By the end of the test period, appropriate settings and detector locations had been found, and focus was on taking data from the BLM detectors as well as from the BPM system. This data can be analysed to find the amount of beam lost at the BLM detector locations. Eventually, this will be used to obtain real-time information about the beam losses, which will allow operators to tune the performance of the accelerator while it is running.

During the CTF-3 test run, beam was sent to the TBL during one day per week. The data was taken parasitically while other experiments were running, and since the machine settings could change as the other experiments progressed, few measurements were done under the same conditions. The data that will be analysed was taken during one day with stable beam conditions and where few changes were made in the machine settings.

9.1 Conditions

The data to be analysed was taken at the 15th May, 2013. At this date, the diamond detector had been installed, valid settings had been found for all three localized detectors, and the Cherenkov fiber had been moved and was located 28 cm above the beam line, rather than in the cable tray. The length of the beam train was 150 ns with an average current of 16 A, and due to good beam conditions the losses were relatively low. Using an oscilloscope, some data was taken with better resolution than provided by the A/D converter and data acquisition system. Several thousand BLM signals were also taken during the day, together with BPM data.

9.2 Localized detectors

During the previous weeks, tests at CTF-3 had been focused on the combination scheme, and the beam intensity had been increasing as the tests progressed. This led to some

detectors saturating, and to prevent this the detectors were moved to be 20 to 40 cm below the beam line. The detector position is shown in figure 9.1, and the location of the detector sensitive region is given in table 9.1. The detectors were installed after quadrupole number 8.

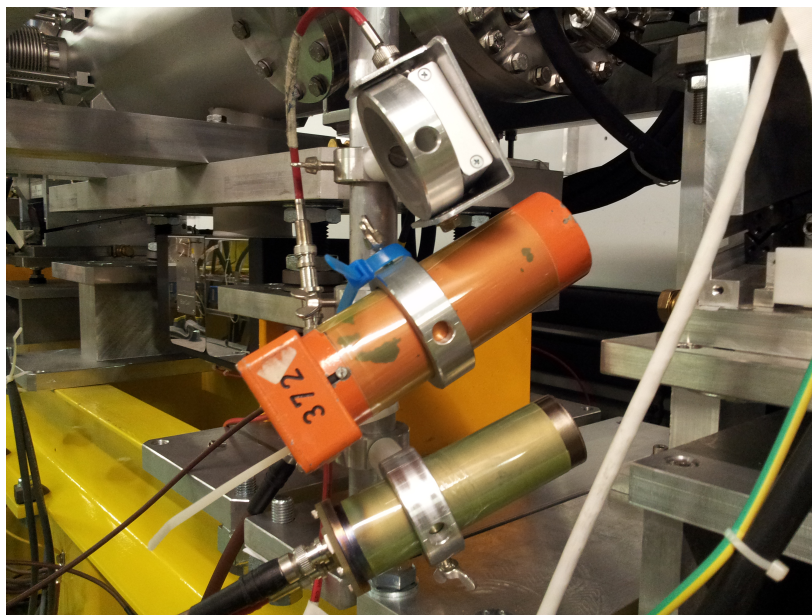


Figure 9.1: Position of the localized detectors. The gray box on top is the diamond detector, the orange cylinder below is the ACEM, and the beige cylinder at the bottom is the PEP-II.

A total of 46 data samples were taken with the oscilloscope for the localized detectors. The average BLM signal is shown in figure 9.2. It can be seen that both the PEP-II and the diamond detector show some time structure of the loss, while the ACEM does not give this information. It takes 40 ns for the electrons in the photomultiplier tubes used to traverse the dynodes, so the PEP-II and the ACEM signal is 40 ns after the diamond signal, which is almost instantaneous.

By integrating the signal, and using the fact that a 50Ω resistance terminated the signal, the total charge produced by the detectors can be calculated. The result is shown in table 9.2.

Combining this with the detector response given in tables 8.7 and 8.8, the total amount of beam lost at the quadrupole can be calculated. The beam loss, calculated from both

Detector	Horizontal distance to beam line [cm]	Vertical distance to beam line [cm]	Distance from quadrupole end [cm]
Diamond	20	20	10
ACEM	12.5	26	7
PEP-II	15	36	8

Table 9.1: Location of the detector front faces.

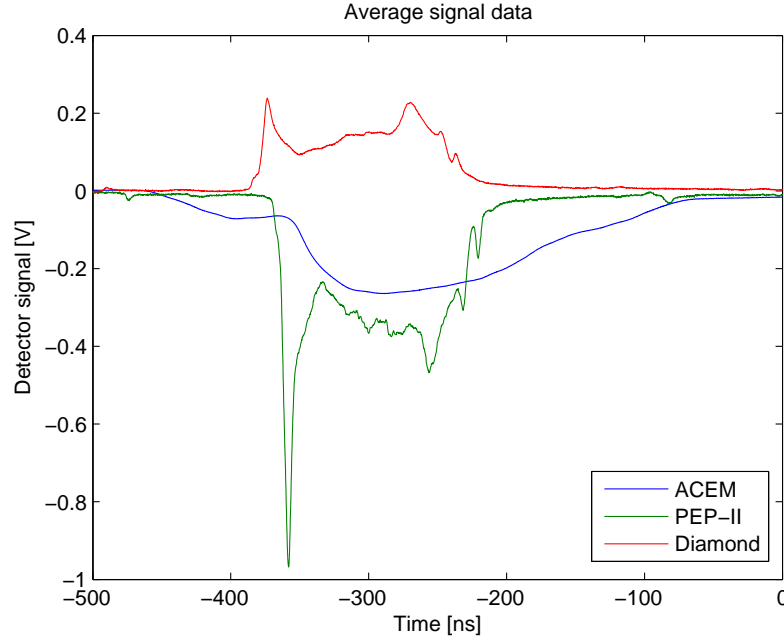


Figure 9.2: Average BLM signal taken over 46 samples.

electron fluence and dose response, is given in table 9.3.

In total, the amount of beam lost by the different detectors is within one order of magnitude from each other. For loss estimations based on electron fluence considerations, that are the most accurate, all detectors suggest a similar amount of beam lost. The PEP-II estimate based on dose has large errors due to the difficulty of simulating the dose at the detector sensitive region.

9.3 Cherenkov fiber

The Cherenkov fiber was originally installed in a cable tray running at some distance from the TBL. Based on simulations, as well as preliminary data taken by the fiber, it was found that a fiber at this distance would not be sensitive enough to give useful data. The fiber was moved to 28 cm above the beam line in early May, and all data analysed here is for a fiber installed close to the beam line.

Detector	Average measured charge
ACEM	$1.21 \cdot 10^{-9} \pm 3.9 \% \text{ C}$
PEP-II	$1.25 \cdot 10^{-9} \pm 13 \% \text{ C}$
Diamond	$4.20 \cdot 10^{-10} \pm 15 \% \text{ C}$

Table 9.2: Measured charge generated by the localized detectors.

Detector	Loss based on electron fluence [mA]		Loss based on dose [mA]	
	Range	Median	Range	Median
ACEM	23 - 135	51	15 - 100	34
PEP-II	10 - 120	30	4 - 540	13
Diamond	9 - 50	20	8 - 50	19

Table 9.3: Beam losses at quadrupole 8 measured by the BLM detectors.

The signal from the TBL fiber is led out of the experimental hall by other fibers, and Cherenkov photons can be generated in these fibers as well. To measure the amount of Cherenkov photons generated in the signal cables, two additional fibers run parallel to the signal fibers, and these are not connected to anything in the hall. Since they run parallel to the signal fiber they will pick up the same background signal, that can be measured separately. The idea is to subtract the background from the signal generated by the TBL, resulting in a signal containing only information about TBL losses. Unfortunately, the fiber for the downstream background was damaged before the TBL fiber was moved, so no estimate was available on the downstream background signal. During earlier measurements only a low downstream background was detected that could be neglected. The upstream background signal was however available, and was big enough that it must be taken into account.

Using an oscilloscope, the fiber signals were measured for 29 bunch trains passing through the TBL. The average signal is given in figure 9.3. The upstream signal and background is shown in greater detail in figure 9.4. It can be seen that the upstream background closely correspond to the early upstream signal, making it possible to subtract the background. It can also be seen that the upstream signal consists of two plateaus of 150 ns, separated by about 200 ns, where the first plateau matches the background signal. Since the plateau width matches the beam length, the plateaus are consistent with losses at single locations. The time it takes the beam to traverse the TBL is about 75 ns, and the time needed for the signal to return through the TBL fiber is about 3/2 of this, so the time difference between a loss at the beginning of the TBL and one at the end of the TBL is around 180 ns. The signal is thus consistent with large losses at single locations before and after the TBL, with the actual TBL signal being drowned in this background. For this reason, the fiber signal may not be a good indicator of the losses at the TBL.

For comparison with the localized BLM detectors, the downstream signal and the upstream one with the known background subtracted was integrated. The result is shown

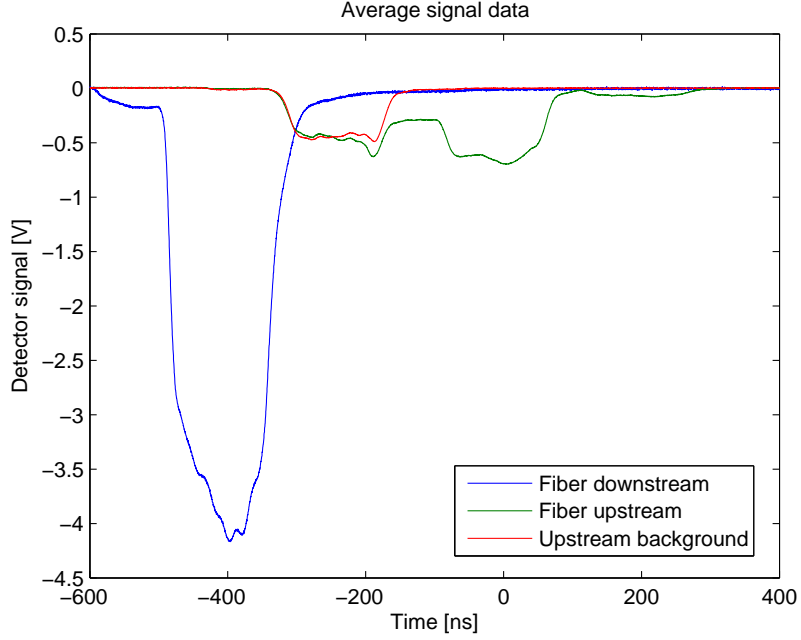


Figure 9.3: Average fiber signals taken over 29 samples.

in table 9.4.

Detector	Average measured charge
Upstream	$5.15 \cdot 10^{-10} \pm 4.4 \% C$
Downstream	$2.36 \cdot 10^{-9} \pm 2.4 \% C$

Table 9.4: Measured charge generated by the fibers, with background removed.

Combining this with the response data from table 8.9, the total beam loss in the TBL can be calculated. The result is shown in table 9.5.

Given that the losses at one quadrupole is about 10 to 100 mA according to the localized detectors, if the losses at each of the 16 quadrupoles are roughly the same the fiber should measure a loss of about 160 to 1600 mA. The calculated values are consistent with this, but as noted earlier, if the main portion of the loss occurs before and after the TBL, the measured losses by the fibers would be lower than the localized detectors would suggest. The effect of losses outside of the TBL on the fibers has not been simulated, and there are no localized detectors installed that can measure these losses.

9.4 BPM

The BPM data was taken simultaneously with the BLM data, and was obtained from the data acquisition system. Although the BPMs are intended to give the beam position in

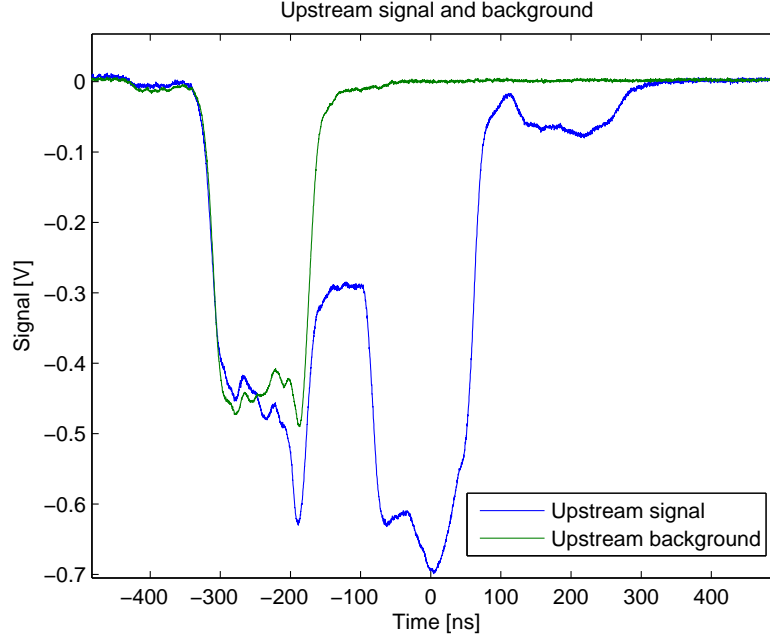


Figure 9.4: Average upstream fiber signals taken over 29 samples.

Detector	Beam loss in the TBL [mA]	
	Range	Median
Upstream	140 - 2300	370
Downstream	120 - 980	260

Table 9.5: Measured beam losses in the TBL by the fibers, with background removed.

the vacuum pipe, it can also be used to give the total charge passing through it. The CTF-3 operators have previously been using this information to give an estimate of the beam losses, to see how different machine settings affect the stable transport of the beam. The BPM data that was saved was from the 16 BPMs at the TBL, one additional BPM before and one after the TBL, and one in the transfer line.

To get the amount of beam lost between each TBL module, the average beam current through each BPM was calculated. The result is shown in figure 9.6. The total current measured by the BPM is accurate to 5 %, which is an error of about 0.8 A. This is much larger than the beam loss calculated from the BLM signals, so finding the amount of beam lost per quadrupole through the BPM system does not work well for low losses. For beam conditions with higher losses the BPM system can give a rough estimate of how much beam has been lost, but for lower losses it is not precise enough for this task. A linear least square fit suggest an average beam loss of 24 mA per quadrupole in the TBL.

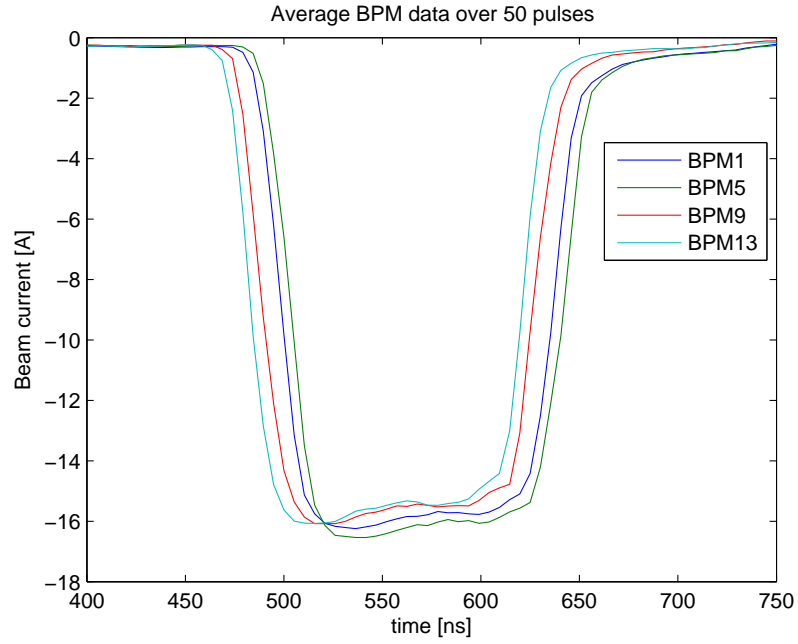


Figure 9.5: BPM data from four different BPMs in the TBL.

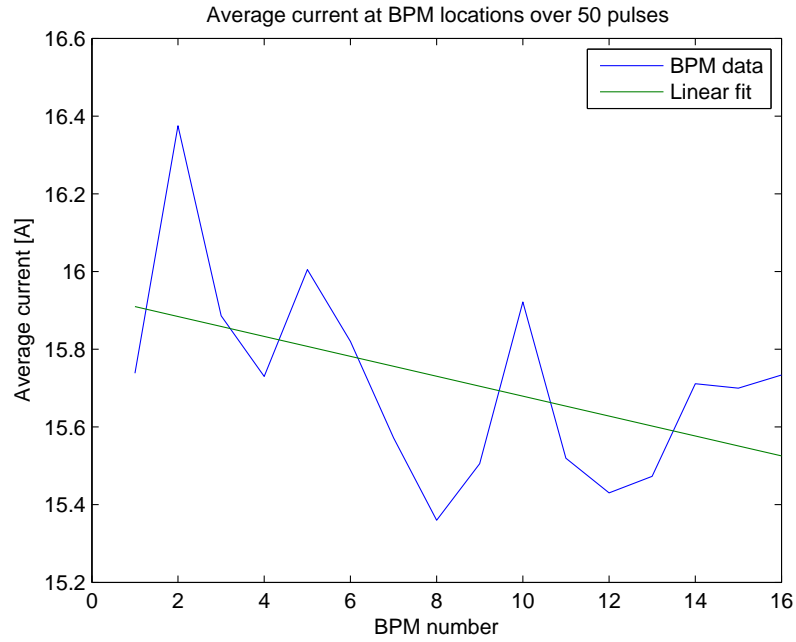


Figure 9.6: Average beam current measured by the TBL BPMs, and a linear least square fit of the BPM data.

Chapter 10

Conclusions

The purpose of this work has been to investigate the performance of the BLM detectors installed at the TBL, and develop the BLM system. This has been done by simulating the secondary shower particles that can be measured by the detectors, as well as by comparing simulations with measurements performed at the TBL. The FLUKA model has been built for the TBL to include a detailed representation of the main beamline components and quadrupole magnetic fields in the FODO lattice. Custom routines were developed which can be easily modified for various loss scenarios and for various detector arrangements. Measurements revealed that the losses determined from three BLM types, ACEM, PEP-II and diamond, installed at the same longitudinal position along the TBL beam were consistent. The Cherenkov fiber BLM system requires further investigation, where measurements are to be taken using a better fiber arrangement to reduce the background signal. However the first results are not inconsistent with the other BLMs. The BPMs are limited by their resolution. However the BLM measurement of the current lost is consistent with the upper limit of losses based on a best line fit of the BPM signals along the TBL averaged over multiple pulses.

The main contribution to the uncertainty in the loss estimate comes from the detector sensitivity calculations. A better estimate of the sensitivity could reduce the uncertainty by a factor of about three. The detectors have mainly been used previously to estimate relative losses, and they are calibrated to give the same output signal when subjected to the same sample radiation. More precise information is required to estimate the number of particles detected, such as how the sensitivity is affected by the particle energy and the angle at which it enters the detector. For the chosen TBL BLM technology, a detailed study of the detector response to known radiation should be performed.

Another contribution to the uncertainty of the loss estimation is the uncertainty in the loss conditions. The PETS can affect the stability of the beam, causing losses at other locations than the quadrupoles. A careful study of the beamline optics and the effects of the PETS is required to find where the losses actually occur. This will allow for more accurate simulations, and better estimates of the secondary particle shower that a detector can measure.

Throughout the measurements, the PEP-II and the diamond have demonstrated a sufficient time resolution to see the time structure of the losses. The ACEM has not been

able to see this structure during these measurements, and the resolution of the Cherenkov fiber is ongoing research. Both the PEP-II and diamond detector perform better than the ACEM in terms of temporal resolution or sensitivity, and either one is a suitable choice for replacing the ACEM that is no longer manufactured. The final choice of BLM detector technology require a further investigation on cost, availability and radiation hardness.

Bibliography

- [1] J. Hauptman. *Particle Physics Experiments at High Energy Colliders*. John Wiley & Sons, 2011.
- [2] J. Ranft, A. Fasso, A. Ferrari and P.R. Sala. FLUKA: a multi-particle transport code, CERN-2005-10, INFN/TC-05/11.
- [3] G. Battistoni et al. The FLUKA code: Description and benchmarking. Proceedings of the Hadronic Shower Simulation Workshop 2006, Fermilab, 6-8 September 2006.
- [4] K. Wittenburg. Beam loss monitors, 2009. Presented at CAS - CERN Accelerator School: Course on Beam Diagnostics.
- [5] J. Beringer et al. Review of particle physics. *Phys. Rev. D*, 86:010001, Jul 2012.
- [6] L. Evans and P. Bryant. LHC Machine. *Journal of Instrumentation*, 3(08):S08001, 2008.
- [7] R. Assmann, M. Lamont, and S. Myers. A Brief History of the LEP Collider. *Nucl. Phys. B, Proc. Suppl.*, 109(CERN-SL-2002-009-OP):17–31. 15 p, Apr 2002.
- [8] The ILC collaboration. <http://www.linearcollider.org/ILC>.
- [9] The CLIC collaboration. <http://clic-study.org/>.
- [10] G. Guignard (Editor). *A 3 TeV e^+e^- Linear Collider Based on CLIC Technology*. CERN, Geneva, 2000.
- [11] A Multi-TeV linear collider based on CLIC technology: CLIC Conceptual Design Report, edited by M. Aicheler, P. Burrows, M. Draper, T. Garvey, P. Lebrun, K. Peach, N. Phinney, H. Schmickler, D. Schulte and N. Toge, CERN-2012-007.
- [12] The Linear Collider Collaboration. <http://www.linearcollider.org/>.
- [13] Next generation particle accelerator is ready for construction International Linear Collider publishes its Technical Design Report. Press release. <http://press.web.cern.ch/press-releases/2013/06/next-generation-particle-accelerator-ready-construction-international-linear>.

- [14] M Sapinski, B Dehning, EB Holzer, M Jonker, S Mallows, T Otto, and C Welsch. Requirements of CLIC Beam Loss Monitoring System. (CERN-ATS-2010-105):3 p, Jun 2010.
- [15] S Mallows. Review of the radiation levels in the CLIC tunnel, Presented on the CLIC TBM WG on 28 March 2012.
- [16] J. Hoorne. Cherenkov Fibers for Beam Loss Monitoring at the CLIC Two Beam Module. Master’s thesis, Technischen Universität Wien, 2012.
- [17] S Bettoni, E Adli, R Corsini, A Dabrowski, S Dbert, D Manglunki, P Skowronski, and F Tecker. Achievements in CTF3 and commissioning status. (CERN-ATS-2009-082. CLIC-Note-785):4 p, Oct 2009.
- [18] E Adli, A-E Dabrowski, S Dobert, M Olvegaard, D Schulte, I Syratcev, and Reidar Lillestol. Experimental Program for the CLIC test facility 3 Test Beam Line. Jun 2010.
- [19] W. Leo. *Techniques for Nuclear and Particle Physics Experiments*. Springer-Verlag, second revised edition edition, 1994.
- [20] Hamamatsu Photonics K.K. Photomultiplier Tubes and Assemblies for Scintillation Counting and High Energy Physics, 2009.
- [21] J. Bosser and G. Ferioli. Comparative test results of various beam loss monitors in preparation for LHC. Technical report, CERN, 1999.
- [22] M. Palm. Performance test of ACEM-detector. Presentation available at http://www.hep.princeton.edu/~mcdonald/mumu/target/Palm/palm_acem.pdf.
- [23] A. Fisher. Instrumentation and diagnostics for PEP-II. *AIP Conf.Proc.*, 451:95–109, 1999.
- [24] M. Mikuz, D. Asner, M. Barbero, V. Bellini, V. Belyaev, et al. Diamond detectors. *PoS*, VERTEX2010:024, 2010.
- [25] E. Berdermann et al. Diamond detectors for hadron physics research. *Diamond and Related Materials*, 19(56):358 – 367, 2010.
- [26] M. Pomorski. *Electronic Properties of Single Crystal CVD Diamond and its Suitability for Particle Detection in Hadron Physics Experiments*. PhD thesis, Fachbereich Physik der Johann Wolfgang Goethe Universität in Frankfurt am Main, 2008.
- [27] S. Mallows, E.B. Holzer, and J. van Hoorne. Fiber based BLM system research and development at CERN. Technical report, CERN, 2012.
- [28] E.B Holzer et al. Development, production and testing of 4500 beam loss monitors. 2008. Proceedings of EPAC08, Genoa, Italy.

- [29] D. McComick, R. Gearhart, Robert Gibbs Jacobsen, T. Jenkins, R. Nelson, et al. Long Ion Chamber Systems for the SLC. *Conf.Proc.*, C8903201:1531, 1989.
- [30] M Gasior. An inductive pick-up for beam position and current measurements. (CERN-AB-2003-053 BDI), Jun 2003.
- [31] V.Vlachoudis. Flair: A powerful but user friendly graphical interface for FLUKA, 2009. Proc. Int. Conf. on Mathematics, Computational Methods & Reactor Physics (M&C 2009), Saratoga Springs, New York.
- [32] L. Fernandez-Hernando, V. Cindro, C. Ilgner, A. Macpherson, A. Oh, H. Pernegger, T. Pritchard, R. Stone, and S. Worm. Development of a beam condition monitor for use in experiments at the cern large hadron collider using synthetic diamond. In *Instrumentation and Measurement Technology Conference, 2004. IMTC 04. Proceedings of the 21st IEEE*, volume 3, pages 1855–1859 Vol.3, 2004.
- [33] M. Zingl. Longitudinal Resolution of Cherenkov Fibers. Technical report, CERN, 2013.